Journal of Polymers and the Environment (2026) 34:63
https://doi.org/10.1007/s10924-026-03790-x

ORIGINAL PAPER

Epoxy Latent Systems for Novel Hybrid 3D Printed Metal/CFs Reinforced Composite Joint Disassembly via Chemical Recycling

Lorena Saitta[1] · Sandro Dattilo[2] · Claudio Tosto[1] · Valentina Giglio[2] · Paolo Maria Riccobene[2] · Ignazio Blanco[1,3] · Alberta Latteri[1] · Gianluca Cicala[1,3]

Received: 14 July 2025 / Accepted: 30 January 2026

Abstract

This study presents the chemical, thermal and mechanical characterization of two bio-based and fully-recyclable epoxy latent resins derived from pine oil, engineered to meet high-performance mechanical and thermal specifications for advanced composite applications. The characterized latent epoxy resins exhibited glass transition temperature (T_g) values ranging between 90 and 120 °C, flexural strength and modulus values within the range of 35–110 MPa and 2.5–3.2 GPa, respectively, making them suitable for structural applications. One of the latent epoxy resin was further employed in the fabrication of a hybrid joint comprising metal and CFs reinforced composites characterized by an average ILSS of 11.9 MPa and a maximum load of 1429.2 N, due to a good mechanical interlocking at the metal/CFs interface. Due to its latent curing behavior, the epoxy resin remains stable until exposed to elevated temperatures ($\geq$80 °C), at which point cross-linking is initiated. This property affords an extended pot life and improved control during application and assembly. This feature makes the system especially attractive for hybrid manufacturing approaches, where the extended open time supports accurate positioning of fibers and metal inserts. Furthermore, the epoxy resin was cross-linked by using a cleavable amine hardener to achieve full recyclability, so enabling disassembly under mild acidic controlled conditions. This property facilitated the full recovery of constituent raw materials through a targeted chemical recycling process, achieving a 100% recovery yield. The proposed system offers a sustainable alternative to conventional thermoset-based hybrid metal/CFs composite manufacturing and end-of-life management. This class of hybrid joints can find industrial applications in aerospace and automotive sectors, in electronic and optical applications, in sports equipment and biomedical devices, for the manufacturing of next-generation structural solutions, with enhanced performance and versatility, by also supporting the global shift toward circular design and responsible material use.

Keywords Fiber reinforced composites · Hybrid joints · 3D printing · Recyclable thermosets · Chemical recycling · Bio-based thermosets

---

✉ Lorena Saitta
lorena.saitta@unict.it

Sandro Dattilo
sandro.dattilo@cnr.it

Claudio Tosto
claudio.tosto@unict.it

Valentina Giglio
valentina.giglio@cnr.it

Paolo Maria Riccobene
paolomaria.riccobene@cnr.it

Ignazio Blanco
iblanco@unict.it

Alberta Latteri
a.latteri@unict.it

Gianluca Cicala
gianluca.cicala@unict.it

[1] Department of Civil Engineering and Architecture, University of Catania, Via Santa Sofia 64, Catania 95125, Italy

[2] Institute for Polymers, Composites, and Biomaterials CNR-IPCB, Via Paolo Gaifami 18, Catania 95126, Italy

[3] INSTM-UDR CT, Viale Andrea Doria 6, Catania 95125, Italy

Introduction

Nowadays there is a growing demand for multi-materials, such as metal-polymer and metal-composite hybrid structures (MMHSs), in several fields including aerospace [1, 2], sea transportation [3, 4], automotive [5–7], and healthcare [8]. The adoption of MMHSs in transportation industries represents a pivotal opportunity to reduce the product's weight without compromising structural performance [9]. Indeed, for example, this kind of structures enables a dramatic reduction in fuel consumption for vehicles driven by internal combustion engines as well as an increase in fuel efficiency for electric vehicles [10].

Typical techniques for assembling MMHSs include mechanical fastening via riveting and bolting [11], welding or fusion bonding [12], interlocking or crimping [13–15]. However, these strategies are characterized by a common concern related to their joining regions: these interfaces act as structural discontinuities, where stress concentrations can arise and create vulnerable zones prone to early failure [16]. To overcome this issue, adhesive bonding is an effective alternative joining method for hybrid structures because it can connect similar or dissimilar substrates without causing damage, which is particularly advantageous for composite components in lightweight applications [17]. A wide variety of structural adhesives are available for such applications, including epoxies, acrylics, urethanes, and cyanoacrylates, each offering distinct chemistries and performance ranges [18, 19]. Their properties can be tailored through additives to adjust viscosity and curing rate [20, 21], or stiffness to meet specific design requirements [22, 23].

Among these options epoxy adhesives provide the broadest range of characteristics and the best overall performance on bonding metals and thermoset composites [17, 24]. Epoxy-based adhesives are especially valuable in this context, as their modulus helps to accommodate stiffness mismatches between metals and carbon fibers (CFs) reinforced composites while efficiently transferring loads through shear, which is the primary stress mode in bonded joints. Despite challenges such as peel stresses, edge effects, and stress concentrations in configurations like lap joints, epoxy matrices have proven reliable in maintaining joint performance and durability. Building on this foundation, epoxy latent resins represent an advanced solution, combining the mechanical strength and durability of epoxies with controlled curing behavior, that is an advantage for assembling complex or large-scale lightweight hybrid joints. In fact, these formulations remain stable at ambient conditions but cure rapidly under thermal activation, enabling simplified handling and integration into automated workflows [25]. Latency is particularly relevant in hybrid assemblies, where delayed curing allows precise positioning of dissimilar components or handling complex assemblies before joint consolidation [23, 26–28]. Furthermore, tailoring the curing kinetics and latency of the epoxy system allows for greater control during assembly, making it compatible with automated or additive manufacturing (AM) workflows. Within this field, hybridization with AM is particularly attractive: 3D printing can deliver geometrically complex interfaces, precise bond-line control, and tailored load paths that are otherwise difficult to achieve with conventional techniques [29–34].

However, the use of thermoset-based MMHSs systems is arising environmental concerns, since they do not allow for chemical recyclability or reprocessability once cured and, moreover, derives from petroleum-based raw materials. For this reason, thermoplastic composite materials are commonly chosen over thermosetting one, since they provide strong environmental recovery [35]. However, this drawback is being overcome by the use of bio-based cleavable epoxy–amine resins. Among these, Recyclamine™ technology introduces acid-labile acetal linkages into the crosslinked network [36–38]. Once cured, the material behaves as a robust thermoset, but under mild acidic conditions the network can be selectively cleaved into soluble oligomers while leaving intact reinforcing fibers [36, 39] and reusable oligomer [36, 40–42]. Thus by combining bio-based epoxy feedstocks with recyclable amines, the result consists in achieving bio-epoxies providing the opportunity to align with circular-economy principles.

Despite these technological advances, a critical research gap remains: the integration of bio-based, recyclable latent epoxy systems into AM-enabled MMHS joint architectures has not yet been systematically explored for the best of our knowledge. Furthermore, the combined effects of cure latency, curing kinetics, and chemical recyclability on the mechanical performance of load-bearing hybrid joints remain largely unexplored in the state-of-the-art. This is also confirmed by the recent comprehensive review on fiber-reinforced polymer/metal hybrid structures published by D. Wang et al. [43], which highlights that the long-term structural performance of MMHSs is strongly governed by the integrity of their interphases and joint architectures, and emphasizes that, despite significant progress in surface treatments and conventional joining approaches, persistent challenges remain in achieving robust, durable, and design-flexible hybrid joints, particularly when advanced manufacturing routes and sustainable material systems are considered. This analysis clearly indicates the need for new joint concepts integrating tailored interphases, innovative manufacturing strategies, and recyclable systems. Hence, within this context, the present study addresses this gap by developing and characterizing bio-based, recyclable latent epoxy systems formulated from epoxidized pine-oil derivatives and commercial Recyclamine™ R*301/R*401 hardeners, and by demonstrating their integration into additively manufactured MMHS hybrid joints combining a 316L stainless-steel insert, a CFRP layer, and a Polyvinylidene fluoride (PVDF) core. A novel manufacturing route is proposed that integrates AM with vacuum-assisted hand lay-up, enabling the fabrication of structurally efficient and chemically recyclable hybrid joints.

The novelty of this work lies in:

- the development of fully recyclable, bio-based latent epoxy adhesives for hybrid joints;
- their integration into AM-enabled MMHS architectures;
- the systematic evaluation of their suitability for load-bearing hybrid assemblies;
- the demonstration of MMHS disassemblability and 100% material recovery efficiency.

The latter proposed strategy is based on the use of cleavable amine curing agents for the epoxy adhesive employed in the MMHS joints. By intrinsically embedding chemical recyclability into the polymer network, this approach enables the selective depolymerization of the cured epoxy under mild conditions, allowing for the effective recovery of both the polymer matrix and the reinforcing fibres. As a result, the proposed environmentally friendly solution offers a significant advantage over conventional composite recycling routes, such as the recent microwave-assisted pyrolysis (MAP) technology proposed by M.Y. Shen et al. [44], that focus on fibre recovery with matrix loss or degradation.

These advancements enable a broad range of application opportunities across multiple industrial sectors. In aerospace, lightweight, reconfigurable, and recyclable hybrid joints can significantly reduce material waste and improve maintenance efficiency [45, 46]. In automotive manufacturing, the integration of structural composites with metals through freeform hybrid joints enhances structural performance while facilitating end-of-life separation and recovery of valuable materials [47, 48]. Consumer electronics can benefit from the miniaturization and customization enabled by additively manufactured hybrid assemblies [49, 50]. In this context, epoxy matrix-based materials, particularly bisphenol A-type diglycidyl ether (BPA) systems, remain foundational in electronic packaging applications such as solder pastes, direct chip attachment, and underfill adhesives due to their excellent insulation and moldability [51, 52], although their high coefficients of thermal expansion and limited thermal stability can lead to delamination and substrate deformation during service [53, 54]. Sports equipment and biomedical devices can exploit the tailored mechanical properties and recyclability of these materials to enable user-specific designs and improved environmental compliance [55–57]. Finally, in advanced optical technologies, hybrid organic–inorganic assemblies provide a unique combination of mechanical robustness, thermal stability, and tunable optical properties [58, 59], supporting demanding optical applications that require controlled refractive index [60, 61] and light transmission characteristics [62, 63–66].

Materials and Methods

Materials

The two fully-recyclable and bio-based epoxy resins used in this work are bicomponent systems both composed of a bio-based prepolymer, named PolarBear, with the 28% of bio-content derived from pine oils, which differ each other for the used hardener. In fact, two different latent hardeners were used, i.e., Recyclamine™ R*301 and Recyclamine™ R*401. The latter are classified as curing agents with latent behavior, that is *dormant* systems in storage conditions at room temperature (RT) but quickly reactive under polymerization conditions, i.e., at high temperatures, generally above 100 °C. This kind of epoxy system is beneficial when it is necessary to have a controllable usage window during the production process, being able to trigger the reaction between epoxide and amine by controlling the temperature. Furthermore, the two used hardeners are fully-recyclable. The key factor for their recyclability is based on the presence of acid–cleavable groups within their chemical structure, which can be selectively cleaved under mild acetic conditions.

The epoxy prepolymer (PolarBear) was purchased by R*CONCEPT (Barcelona, Spain), while the amines Recyclamine™ R*301 and Recyclamine™ R*401 were provided by Aditya Birla Group (Mumbai, India).

For the hybrid 3D printed metal/CFs reinforced composite joint manufacturing, several raw materials were employed. The composite sandwich structure's core was made of Solef® Polyvinylidene fluoride (PVDF) provided by Solvay (Bollate, Italy). The used dry carbon fabric used was a twill 2 × 2 12 K fabric with 600 gsm (grams per square meter) areal weight purchased from Telateks (Tuzla, Istanbul, Turkey). The metallic components (of size 12.6 × 12.6 × 2.0 mm^3) were manufactured using Ultrafuse® 316L stainless steel-based polymer/metal hybrid filaments from BASF (Ludwigshafen, Germany), processed via metal Fused Filament Fabrication (metal FFF) using a Raise3D (Irvine, CA, USA) Forge 1 3D printer. Following printing, the so-called *green parts* underwent catalytic debinding in nitric acid and subsequent sintering (debinding and sintering, D&S) to obtain fully dense metallic components. D&S

processes were outsourced to certified partners of Forward AM, section of BASF [67].

Epoxy Resin Formulation

The two investigated formulations were produced by mechanically mixing the PolarBear with two different recyclable amines as curing agents: Recyclamine R*301 and R*401. The chosen mixing ratios were 27 and 29 phr (per hundred resin), respectively. The mechanical mixing was performed with a planetary mixing Thinky mixer ARV310 (THINKY U.S.A. Laguna Hills), under vacuum conditions, for 3 min and with a rotational speed of 2000 rpm. In this way, a homogeneous mixing was achieved and the epoxy formulations were also degassed.

For each formulation two different curing cycles were investigated. These are reported in Table 1.

The two implemented curing cycles were selected in accordance with the following ratio. The first one (curing cycle *C1*) was investigated for comparison purposes with previous studies [36, 37, 68], where the bio-based epoxy prepolymer PolarBear was mixed with the fully-recyclable amine hardener Recyclamine™ R*101, which does not have a latent behavior. While, the second one (curing cycle *C2*) was determined by analyzing the Differential Scanning Calorimetry (DSC) thermograms of the uncured formulations (see Sect. "DSC results").

The viscosity of the two uncured formulations was measured with a Brookfield Fungilab viscolead series adv viscometer in a temperature range from 25 up to 80 °C and a spindle speed ranging between 30 (at 25 °C), 50 (at 50 °C) and 100 (at 80 °C) rpm. The measured value are reported in Table S1 of the supplementary materials.

Table 1 Developed latent epoxy formulations and curing cycles

Sample ID	Formulation	Mixing Ratio	Curing Cycle ID	Curing Cycle
P_R*301_C1	PolarBear + Recyclamine R*301	100:27	*C1*	25 °C for 24 h + 100 °C for 3 h
P_R*301_C2	PolarBear + Recyclamine R*301	100:27	*C2*	80 °C for 25 min + 140 °C for 4 h
P_R*401_C1	PolarBear + Recyclamine R*401	100:29	*C1*	25 °C for 24 h + 100 °C for 3 h
P_R*401_C2	PolarBear + Recyclamine R*401	100:29	*C2*	80 °C for 25 min + 140 °C for 4 h

Epoxy Formulations Chemical and thermo-mechanical Characterization

Heated Electrospray Ionization Mass Spectroscopy (HESI-MS)

To determine the chemical structure of the two used recyclable amines (R*301 and R*401), heated electrospray ionization (HESI) mass spectra (MS) were acquired on a Thermo Scientific Exactive Plus Orbitrap mass spectrometer (Thermo Fisher Scientific, San Jose, CA, USA) equipped with a heated electrospray ionization (HESI II) source. Analyses were conducted in positive ion mode over an m/z range of 150–1000, with a resolving power of 25000 (FWHM at m/z 200) and a C-trap injection time of 100 ms. Source parameters were configured as follows: capillary temperature, 275 °C; sheath (nebulizer) nitrogen gas flow, 5 arbitrary units; auxiliary gas flow, 1 arbitrary unit; spray voltage, 3.5 kV; capillary voltage, 82.5 V; and tube lens voltage, 120 V. Instrument tuning and calibration in positive ion mode were performed by direct infusion of standard solutions of caffeine (Mr 194.1 Da), MRFA peptide (Mr 423.6 Da), and Ultramark (Mr 1621 Da). Data acquisition and processing were carried out using the Excalibur software package.

Differential Scanning Calorimetry (DSC)

Differential Scanning Calorimetry (DSC) analysis was performed on the uncured formulation to determine the curing cycles that are most compatible with the developed bio-based latent epoxy systems, with the aim to achieve a fully-cured cross-linked network.

For carrying out the calorimetric measurements it was employed a Shimadzu DSC-60 (Shimadzu, Kyoto, Japan) instrument. For each test, a sample of approximately 6 mg was placed inside a 40 µl aluminum sealed crucible and subsequently analyzed. The test was carried out by varying the temperature from 25 °C up to 250 °C at a rate of 5 °C/min in air. Additionally, once the epoxy resins were cured by mean of the selected curing cycles, further DSC tests were performed to determine the curing state. In the end, the latency of the epoxy formulations was investigated by carrying out isothermal DSC of the uncured formulations at 25 °C for 4 h.

Dynamic Mechanical Analysis (DMA)

To determine the glass transition temperature (T_g) for the four types of cured specimens the dynamic mechanical analysis (DMA) was carried out. With the aim to identify the most performing one, as combination of used hardener and implemented curing cycle, a Design of Experiments (DoE) approach was employed. Thus, a 2^2 replicated factorial design was investigated, being the investigated factors (independent variables) the following ones:

- Epoxy resin (named *factor A*) – Categorical factor varied between two levels (a = 2) corresponding to {PolarBear + R*301; PolarBear + R*401};
- Curing cycle (named *factor B*) – Categorical factor varied between two levels (b = 2) corresponding to {*C1*; *C2*}.

The number of replications was fixed at $n = 3$, for a total amount of experimental runs equal to N = a × b × n = 12. The investigated experimental plan is reported in Table 2.

Furthermore, for the collected observations was performed an Analysis of Variance (ANOVA) to investigate the statistical significance of each chosen factor (*A* and *B*) and their interaction (*AB*).

The DMA tests were performed using a dynamic mechanical thermal analyzer TRITEC 2000 (Triton Technology, Leicestershire, UK) on samples having a size of (10 × 6 × 4) mm^3. The tests were run in single cantilever deformation mode, since it is the best one for characterizing the transition from rigid to rubbery behavior of thermosets [69]. The test parameters were set as follow. The temperature interval was varied between 25°*C* up to 180°*C* with a heating rate of 2 °C/min; initial displacement was set at 20 µm; the frequency was set at 1 Hz. The investigated T_g parameter was determined in correspondence of tanδ versus temperature curve's peak and it was expressed as *mean* ± *st.error*.

In the end, by exploiting the information related to the storage modulus, the stiffness of the investigated thermoset networks by varying the used amine and curing cycle was investigated. In fact, the cross-link densities (v) expressed in [$mmol/cm^3$], was calculated by using the following Eq. (1) [70, 71]:

$$v = \frac{E\prime}{3RT} \tag{1}$$

being $E\prime$ the storage modulus at T_g +50 °C, the R gas constant (equal to 8.31 [$J \cdot K^{-1} \cdot mol^{-1}$]), and T the absolute temperature expressed in [K].

Mechanical Characterization: Flexural Tests

The mechanical properties of the developed formulations were determined through flexural tests, in accordance with the standard ASTM D790. The tested specimens had size of (80 × 10 × 4) mm^3. For testing it was employed an Instron 5985 (Instron, Milan, Italy) equipped with a 10 kN load cell and a three-point bend tool was installed on the machine. The tests were carried out under deformation control, at a speed of 2 mm/min with a support span of 64 mm. For each characterized formulation, a number of $n = 5$ samples were tested. The responses considered were the flexural stress at break, the flexural modulus and the flexural strain at break, which were evaluated as *mean* ± *st.error*. For system control and data collection, the Blue Hill 3.61 software (Instron, MA, USA) was used.

With the aim to identify the most performing combination between the used amine (R*301 and R*401) and the implemented curing cycle (*C1* vs. *C2*), even in this case a Design of Experiments (DoE) approach was employed. Thus, a 2^2 replicated factorial design was investigated, being the investigated factors (independent variables) the following ones:

- Epoxy resin (named *factor A*) – Categorical factor varied between two levels (a = 2) corresponding to {PolarBear + R*301; PolarBear + R*401};
- Curing cycle (named *factor B*) – Categorical factor varied between two levels (b = 2) corresponding to {(*C1*; *C2*}.

The number of replications was fixed at $n = 5$, for a total amount of experimental runs equal to N = a × b × n = 20. The investigated experimental plan is reported in Table 3.

An Analysis of Variance (ANOVA) was carried out to study the statistical significance of each chosen factor (*A* and *B*) and their interaction (*AB*).

Thermogravimetric Analysis (TGA)

The thermal stability of the two investigated amines (i.e., Recyclamine R*301 and R*401) was investigated by Thermogravimetric analysis (TGA). While, for the prepolymer PolarBear it was already reported in a previous study [72]. This investigation was essential to identify any degradation process of the epoxy formulations during high-temperature curing. The analyses were conducted using a Shimadzu DTG-60 instrument (Shimadzu, Kyoto, Japan). Each test

Table 2 Experimental plan for DMA. Factors, levels and investigated response

Response	Factor	Symbol	Type	Unit	Level I	Level II
T_g	Epoxy resin	A	Categorical	[-]	PolarBear + R*301	PolarBear + R*401
	Curing cycle	B	Categorical	[-]	*C1*	*C2*

Table 3 Experimental plan for flexural test. Factors, levels and investigated response

Responses	Factor	Symbol	Type	Unit	Level I	Level II
Flexural strength; Flexural modulus; Flexural strain at break	Epoxy resin	A	Categorical	[-]	PolarBear + R*301	PolarBear + R*401
	Curing cycle	B	Categorical	[-]	*C1*	*C2*

was performed on samples of about 5 mg, in air condition with a heating rate of $20°C/min$, and in a temperature interval ranging from 25 up to $150°C$. Temperature and mass calibration were carried out following the procedure provided by the instrument's control software, using a high-purity magnetic standard for Curie temperature and a precisely measured sample for mass. Data acquisition and analysis were done using the TA Instruments software (New Castle, DE, USA). Thermograms showing mass as a function of temperature were recorded for each component analyzed.

Epoxy Formulations Recyclability

Chemical Recycling

Once the most performing latent epoxy system in terms of thermo-mechanical properties was determined, the recyclability of the formulated systems was investigated. In this regard, an already optimized chemical recycling process for this class of amine was implemented [37]. Briefly, 10 g of cured epoxy resin was dissolved in 300 mL of a 75% (*v/v*) aqueous acetic acid solution at 80 °C for 3 h (R*301) and 2 h (R*401). The resulting solution was then concentrated under vacuum (60 mbar pressure) via rotary evaporation at 60 °C until the volume reduced down to 75 mL. To induce the precipitation of the cleaved epoxy resin, 150 mL of an ammonium hydroxide solution, prepared by mixing equal volumes of water and ammonium hydroxide (28–30% NH_3), was added for neutralization. After completing the precipitation, the solid residue was filtered, washed with deionized water, and dried under vacuum at 50 °C for 24 h. The dried residue was then ground into a powder using a mortar and pestle and characterized. The recycled thermoplastic derived from PolarBear + R*301 is defined rTP301 from now on. While, the one derived from PolarBear + R*401 is defined rTP401 henceforth. The chemical recycling process yield was calculated as reported elsewhere [36, 39, 73].

Recycled Thermoplastic Characterization

Matrix-Assisted Laser Desorption/Ionization Time-of-Flight (MALDI-TOF) Matrix-assisted laser desorption/ionization time-of-flight (MALDI-TOF) mass spectrometry was employed to characterize the recycled thermoplastic, as it provides detailed molecular-level information on polymer structure. This technique enables determination of the mass of individual molecules within a mixture of homologues, allowing the structural identification of single macromolecular chains, including both linear and cyclic species. Moreover, MALDI-TOF facilitates the detection of repeat units, end groups, cyclic oligomers, and minor components, making it particularly well suited for assessing the complex chemical composition of recycled polymers.

MALDI-TOF mass spectra for rTP301 and rTP401 were acquired using a Bruker ultrafleXtreme time-of-flight mass spectrometer (Bruker, Billerica, Massachusetts) in reflectron positive ion mode equipped with an Nd: YAG laser (wavelength of 355 nm). The laser had a wavelength of 355 nm with 3 ns pulse and a 2000 Hz firing rate. The mass resolution of MALDI spectra was about 10000 (full width at half maximum, FWHM) and mass accuracy was 1–5 ppm for masses in the range m/z 500–2000 Da. An appropriate amount of samples were dissolved in $CHCl_3$ and mixed with a solution of α-Cyano-4-hydroxycinnamic acid) to obtain a 1:1 wt ratio. 1 µL of each sample/matrix mixture was spotted onto the MALDI sample holder and dried at room temperature to allow matrix crystallization.

Gel Permeation Chromatography (GPC) The molecular weight of the recycled thermoplastics (rTP301 and rTP401) was determined via gel permeation chromatography (GPC). The analyses were performed on a Knauer Azura 6.1 L system equipped with a pump, autosampler, and differential refractive index (DRI) detector, using tetrahydrofuran (THF) as the mobile phase at a flow rate of 0.6 mL min^{-1}. Separation was achieved with a series of four TSKgel SuperH columns (6 mm ID ×150 mm, 3 µm particle size) connected in sequence. Data were acquired and processed with the Clarity-GPC software package (DataApex). Calibration was carried out using poly(methyl methacrylate) (PMMA) standards. For each injection, 50 µL of a polymer solution in THF (approximately 5 mg mL^{-1}) was introduced, with dichlorobenzene (2 µL mL^{-1}) added as a flow marker.

Dynamic Mechanical Analysis (DMA) The T_g value for the recycled thermoplastics (rTP301 and rTP401) was determined via DMA test using a dynamic mechanical thermal analyzer TRITEC2000 (Triton Technology, Leicestershire, UK) in single cantilever mode. They were tested in their powder form using the pocket DMA approach, a proven technique for analysing powders in the pharmaceutical field [74].

Thus, both rTP301 and rTP401 were pressed into a standard stainless steel pocket (purchased from Triton Technology, Leicestershire, UK) to achieve an uniform thickness. The tests were performed in accordance to the following protocol: the sample was stabilized at 25 °C and then heated up to 80 °C at 5 °C/min (first scan) at a frequency of 1 *Hz* and setting an initial displacement of 200 μm; next, by setting the same test conditions, the samples were cooled down naturally and reheated up to 80 °C at 2 °C/min (second scan). Similar DMA characterization techniques were reported elsewhere [38, 75]. The T_g value was determined in correspondence of tanδ versus temperature curve's peak acquired for the second scan.

Thermogravimetric Analysis (TGA) The thermal stability for the recycled thermoplastics (rTP301 and rTP401) was investigated by TGA (TA Instruments Q500, Perkin Elmer Inc., Waltham, MA, USA), under nitrogen flow (60 mL/min), at a heating rate of 10 °C/min, from 50 up to 800 °C, using about 3 mg of sample. Instrument temperature and weight were calibrated by using high-purity magnetic standard for the Curie temperature and some exact weights, respectively, following the calibration procedure by the instrument control software. The TGA system features a sensitivity of 0.1 µg and a weighing precision of ±0.01%, with an isothermal temperature accuracy of ±1 °C. For each sample, weight loss versus temperature was determined.

Attenuated Total Reflection (ATR) Fourier Transform Infrared Spectroscopy (FT-IR) FT-IR-ATR analysis was carried out using a Thermo Nicolet IS50 (Thermo Fisher Scientific, Waltham, MA, USA) with an integrated diamond ATR sampling module. The spectra were collected over 64 scans in the 4000–500 cm^{-1} range, with a resolution of 4 cm^{-1}, at room temperature.

Scanning Electron Microscopy (SEM) The morphological analysis of the recycled thermoplastics (rTP301 and rTP401) was carried out using a scanning electron microscope (SEM) SEM-EVO 15 (Zeiss, Cambridge, UK) equipped with a LaB_6 (Lanthanum Hexaboride) emitter as the electron source, with an electron high tension (ETH) setting of 25 kV. For the purpose, the specimens were pretreated with a gold-sputter coating process, in fact they were covered with a thin gold film using an Agar Sputter Coater AGB7340 (Assing, Italy). Next, micrographs were captured at a magnification of 50×.

Hybrid Joint Manufacturing

The demonstrator serving as a *proof-of-concept* for a demountable hybrid joint of size $(22 \times 15 \times 25)$ mm^3, was developed using the following strategy. A core, acting as the structural element to define the shape of the joint and meeting lightweight requirements thanks to its infill structure, was designed using *Autodesk Fusion360®* and fabricated through Fused Filament Fabrication (FFF) 3D printer Ultimaker S5. Solef® PVDF was selected for its fabrication, as it is resistant to acidic environments and therefore compatible with the chosen chemical recycling process.

Subsequently, a carbon fiber fabric was applied as the skin over the 3D printed core. The fiber-reinforced composite sandwich structure with a bio-based and fully-recyclable latent epoxy matrix was fabricated using a vacuum-assisted hand lay-up process. The metallic elements of the hybrid joint were also manufactured via metal FFF, using 316 L stainless steel, following an optimized D&S procedure [67, 76, 77]. The imposed printing setting are: 240 °C for the printing temperature, 100 µm for the layer height, 105% for the infill density, and 25 mm/s for the print speed. The metallic inserts were integrated into the composite sandwich using the formulated latent epoxy resin and further embedded within the same system using a custom-designed silicone mold. Finally, the entire joint was consolidated using the curing process identified as the most effective in terms of thermo-mechanical properties. The entire hybrid manufacturing process and the final demonstrator are shown in Fig. 1.

Hybrid Joint Characterization

Mechanical Testing: Short Beam Strength (SBS)

The interfacial bonding strength for the hybrid joint was tested via Short Beam Strength (SBS) mechanical test according to the ASTM D2344M. The tested specimens had size of $(40 \times 12 \times 7.5)$ mm^3 and the layers were stratified as follow: PVDF core – CFs composite – 316L insert. For testing it was employed an Instron 5985 (Instron, Milan, Italy) equipped with a 10 kN load cell. The tests were carried out at a speed of 2 mm/min with a support span of 30 mm. A number of $n = 5$ samples were tested. The responses considered were the interlaminar shear strength (ILLS) and the maximum load, which were evaluated as *mean ± st.error*.

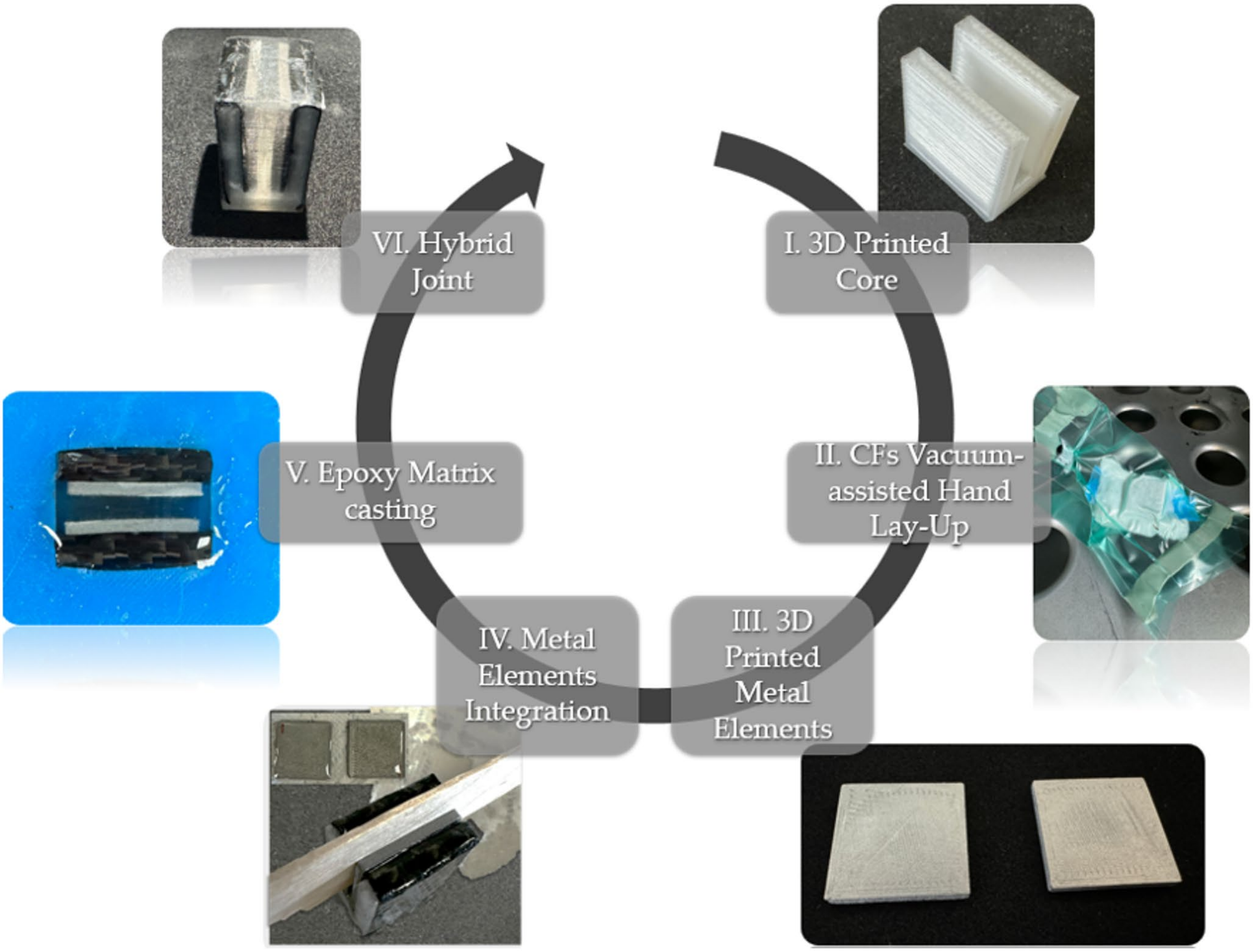

Fig. 1 Schematization for the composite/metal hybrid joint manufacturing process

For system control and data collection, the Blue Hill 3.61 software (Instron, MA, USA) was used.

Adhesion Investigation: Morphological Analysis

To investigate the interfacial bonding and evaluate the presence of potential defects, such as poor adhesion between different layers, a morphological characterization of both the 316L insert/CFs composite and CFs composite/PVDF core interfaces was carried out. For the purposes it was used a Phenom ProX Electronic microscope (Phenom-World BV, Eindhoven, The Netherlands).

Hybrid Joint Disassembly Assessment

Disassembly Via Chemical Recycling

The chemical recyclability as disassembly strategy for the developed novel hybrid 3D printed metal/CFs reinforced composite joint was assessed as *proof-of-concept*. Hence, the employed fully-recyclable hardener is characterized by a chemical structure integrating a cleavable ketal group which aids in selectively cleavage the crosslinked network when treated in mild acid conditions. The latter procedure was used in accordance with previous recyclability studies carried out [36, 37, 39, 68]. Briefly, the joint was immersed in 500 mL of an aqueous acetic acid solution (75% by volume acetic acid and 25% by volume distilled water) at 80 °C for 7 h. Subsequently, the functional elements disassembled within the solution—namely, the 3D printed PVDF core, the metal inserts, and the CFs—were recovered through filtration. On the other hand, the acid solution containing the thermosetting matrix was roto-evaporated at 60 °C and a pressure of 60 mbar, until a more concentrated volume of 75 mL was reached. The latter solution containing the dissolved polymer was neutralized, in accordance with the previously described procedure [37], using an ammonium hydroxide solution, thereby yielding the recycled thermoplastic in the form of a whitish precipitate. The latter was washed with distilled water and dried in a vacuum oven at 50 °C for 24 h.

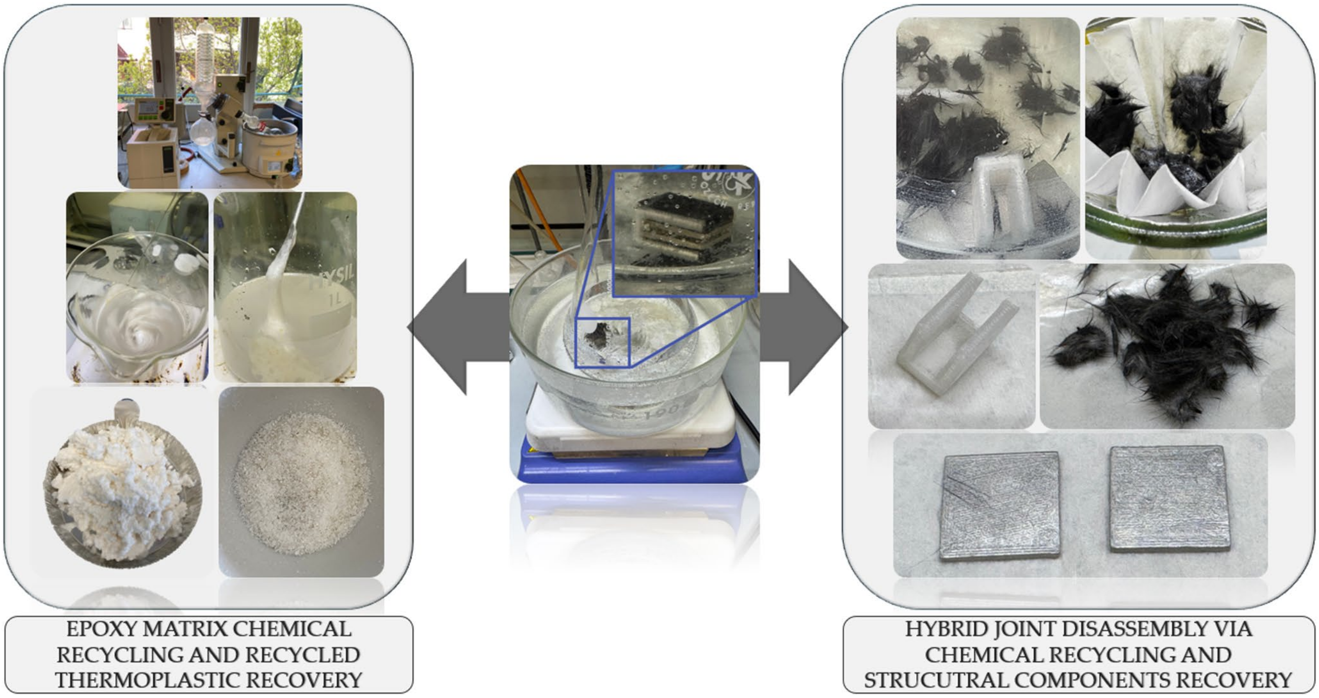

Fig. 2 Schematization for the disassembly procedure of the composite/metal hybrid joint through chemical recycling

Fig. 3 Time evolution of the disassembly process of the hybrid joint through chemical recycling

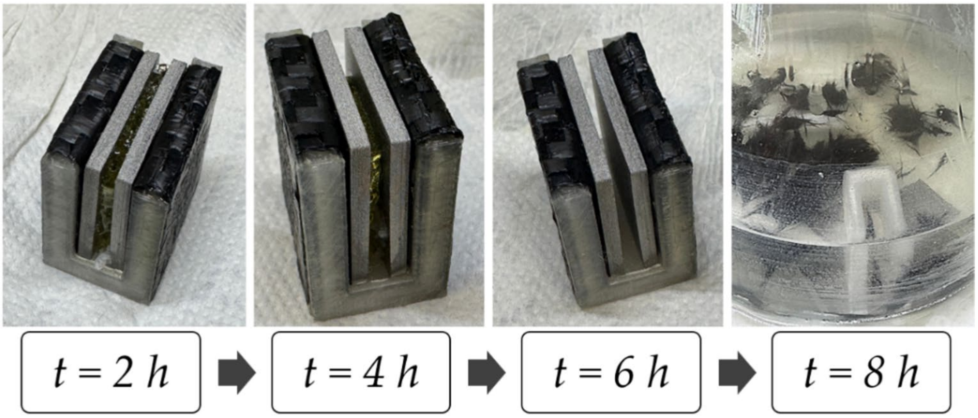

The entire disassembling procedure via chemical recycling process is schematized in Fig. 2.

Figure 3 illustrates the dissolution of the thermosetting matrix over time during the chemical recycling process of the hybrid joint.

Recycled CFs Characterization

The recycled CFs (rCFs) were characterized via thermogravimetric analysis (TGA). This investigation was essential to identify if the rCFs are clean, i.e., if any epoxy matrix residual on the CFs surface is still present, thus suggesting whether a longer duration for the dissolution process is required.

The analysis was conducted using a Shimadzu DTG-60 instrument (Shimadzu, Kyoto, Japan) on a sample of about 3.5 mg, in air atmosphere with a heating rate of 10 °C/min, and in a temperature interval ranging from 25 up to 150 °C. Temperature and mass calibration were carried out following the procedure provided by the instrument's control software, using a high-purity magnetic standard for Curie temperature and a precisely measured sample for mass. Data acquisition and analysis were done using the TA Instruments software (New Castle, DE, USA). Thermograms showing mass as a function of temperature were recorded for each component analyzed.

The rCFs surface quality was also evaluated via morphological analysis, using a scanning electron microscope (SEM) SEM-EVO 15 (Zeiss, Cambridge, UK). For the purpose, the specimens were attached to a stub with carbon tape and then metallized through a sputter-coating process. This process involved depositing a thin gold film using an Agar Sputter Coater AGB7340 (Assing, Italy). Micrographs were captured at a magnification of 50×. The analysis was carried out using a LaB_6 (Lanthanum Hexaboride) emitter as the electron source, with an electron high tension (ETH) setting of 25 kV.

Recovered Metal Insertion Characterization

The Fourier Transform Infrared Spectroscopy (FT-IR) was implemented to ascertain whether the chemical recycling process for the joint disassembly negatively affect the metal elements. A Perkin Elmer Spectrum 100 UATR (Waltham, MA, USA) in attenuated total reflectance (ATR) mode was used for performing the test. The spectra were acquired in the range between 4000 and 650 cm^{-1} with 32 scans and a resolution of 4 cm^{-1}.

Results and Discussion

Chemical and thermo-mechanical Properties of Epoxy Systems

HESI-MS

The spectra acquired from the HESI-MS analyses performed on the amines R*301 and R*401 used as crosslinking agent in the investigated epoxy resins are reported in Fig. 4. The spectra in Fig. 4a and b display a main peaks at m/z 191.17 and 219.21 respectively, which are attributed to 2,2-bis(2-aminopropoxy)propane and 2,2-bis(2-aminobutoxy)propane as protonated ion. This confirms what has been reported in the literature on the structure of the two used amines [78].

DSC Results

The results obtained from the DSC analyses of the uncured epoxy resins are shown in Fig. 5; Table 4.

From the DSC thermograms, the exothermic peak temperature (T_{peak}), corresponding to the maximum curing rate, is lower for the PolarBear + R*301 formulation than for PolarBear + R*401 (114 vs 125 °C). The onset temperature of the exotherm (T_{onset}) is also reduced for the PolarBear + R*301 (83.9 vs 90.7 °C). Moreover, the curing enthalpy (ΔH_{cure}), determined from the area under the exothermic peak, is significantly higher for the formulation PolarBear + R*301 rather than PolarBear + R*401 (418.1 vs 326.9 J g^{-1}), indicating a higher reactivity and greater extent of reaction.

Hence, these results indicate that the R*301-based formulation exhibits faster kinetics and higher reactivity compared to R*401-based one, enabling a denser crosslinked network even when curing is performed at relatively low temperatures (i.e., 100 °C).

The isothermal DSC measurements carried out at room temperature for 4 h (see Fig. 6) confirmed the latent behavior of both formulations. No measurable exothermic signal was detected, and the heat flow remained essentially constant over time, demonstrating the absence of spontaneous curing at ambient conditions.

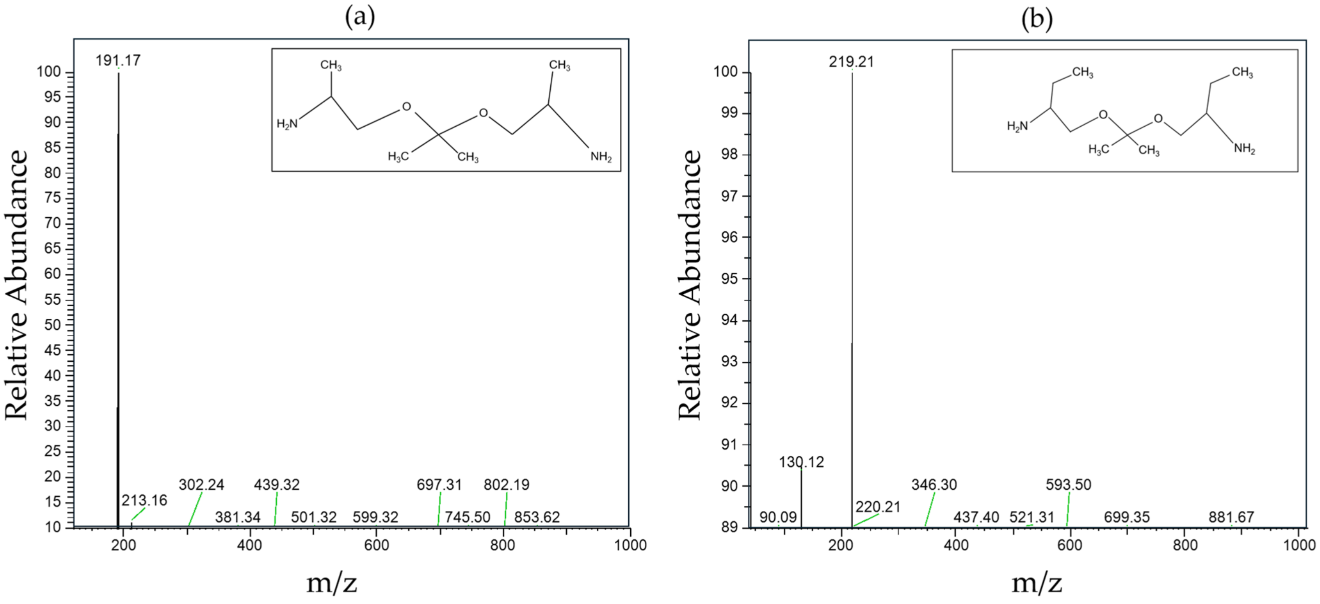

Fig. 4 HESI-MS spectra of the amine R*301 (**a**) and R*401 (**b**)

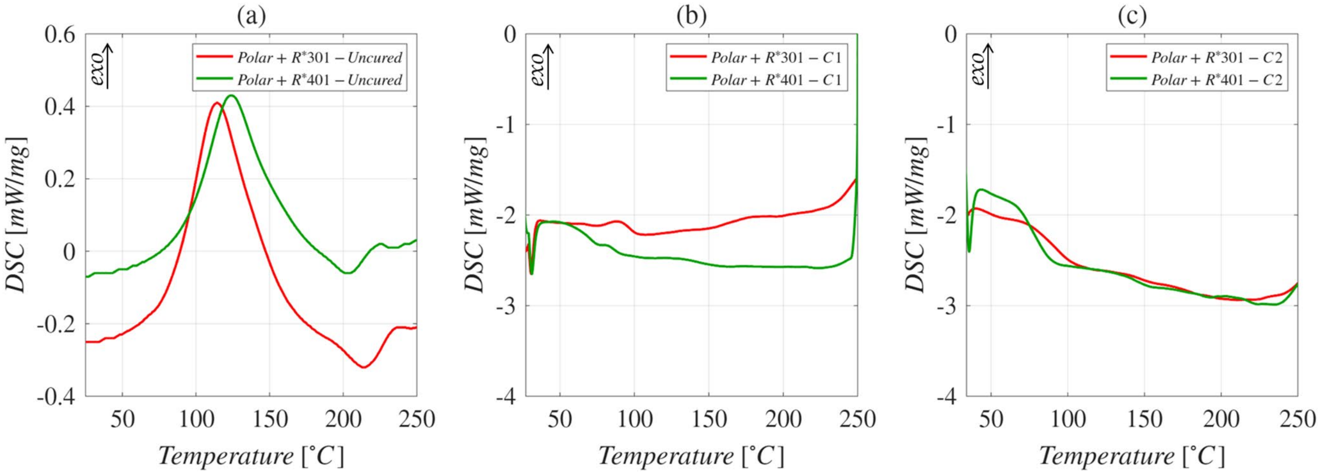

Fig. 5 Acquired DSC thermograms for the two uncured (**a**), cured via *C1* curing cycle (**b**) and cured via *C2* curing cycle (**c**) latent-epoxy resin formulations PolarBear + R*301 (red line) and PolarBear + R*401 (green line)

Table 4 Data obtained from the DSC analysis for the uncured epoxy latent formulations

Formulation	Curing state	T_{peak} [°C]	T_{onset} [°C]	T_{endset} [°C]	ΔH_{cure} [J/g]
PolarBear + R*301	*Uncured*	114.0	83.9	157.9	418.1
PolarBear + R*401	*Uncured*	124.1	90.7	154.3	326.9

Starting from the combination of T_{onset}, T_{peak}, and T_{endset} data (see Table 4), together with the confirmation of latent behavior at room temperature, a second two-step curing cycle (*C2*) was defined: an initial hold near T_{onset} (i.e., at 80 °C for 1 h), followed by a second ranging between T_{peak} and T_{endset} (i.e., at 140 °C for 4 h), to optimize the curing process. The DSC thermograms, acquired to investigate the curing behavior of the two epoxy resins when the curing cycle *C2* is implemented, are reported in Fig. 7. Both systems exhibited a two-step exothermic profile, indicative of a multi-stage curing process. The first exotherm appeared in the range of 50–90 °C, whereas the second, more intense event occurred between 120 and 150 °C. The total reaction enthalpy, obtained by baseline integration of the exothermic peaks, was 7.31 kJ g^{-1} for the formulation PolarBear + R*301 and 7.83 kJ g^{-1} for the PolarBear + R*401 one. In both cases, the first exotherm accounted for approximately 22–23% of the overall heat release (1.60 and 1.79 kJ g^{-1}, respectively), while the remaining 77–78% was released during the second stage (5.71 and 6.04 kJ g^{-1}, respectively). This distribution suggests that only a limited extent of conversion can be achieved at low temperature, whereas the major fraction of curing is completed at elevated temperature.

This result is consistent with the chemical structure of the amines R*301 and R*401 determined via HESI-MS (see Sect. "HESI-MS") which are diamine curing agents, each containing two reactive $–NH_2$ groups. In fact, for such molecules, the cross-linking mechanism typically requires a two-step curing process: (i) an initial cure at moderate temperature (i.e., 40–60 °C) which allows sufficient molecular mobility to initiate network formation without

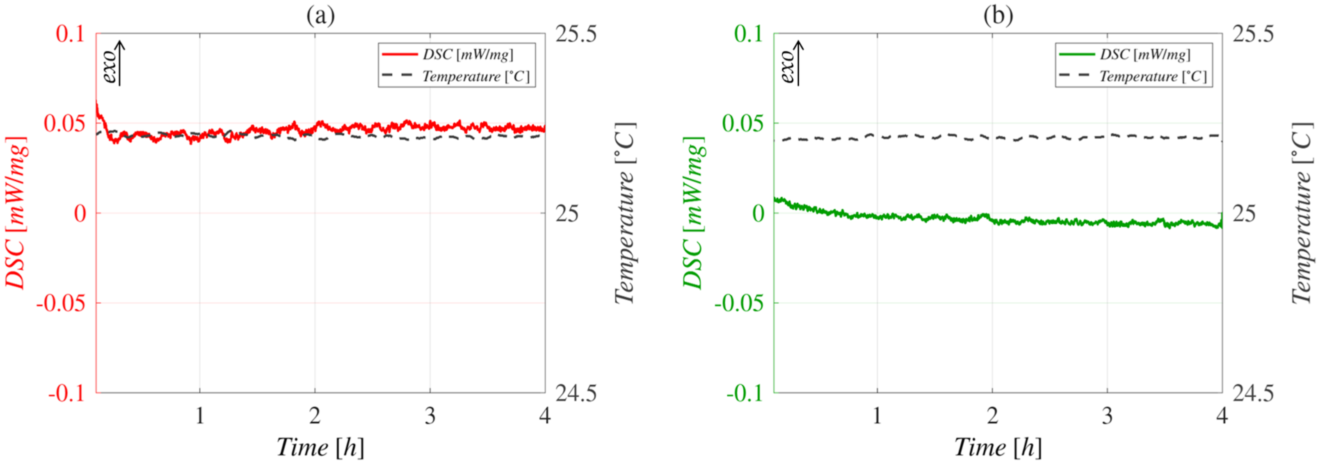

Fig. 6 DSC isothermal thermograms acquired for the two uncured epoxy resins PolarBear + R*301 (**a**) and PolarBear + R*401 (**b**)

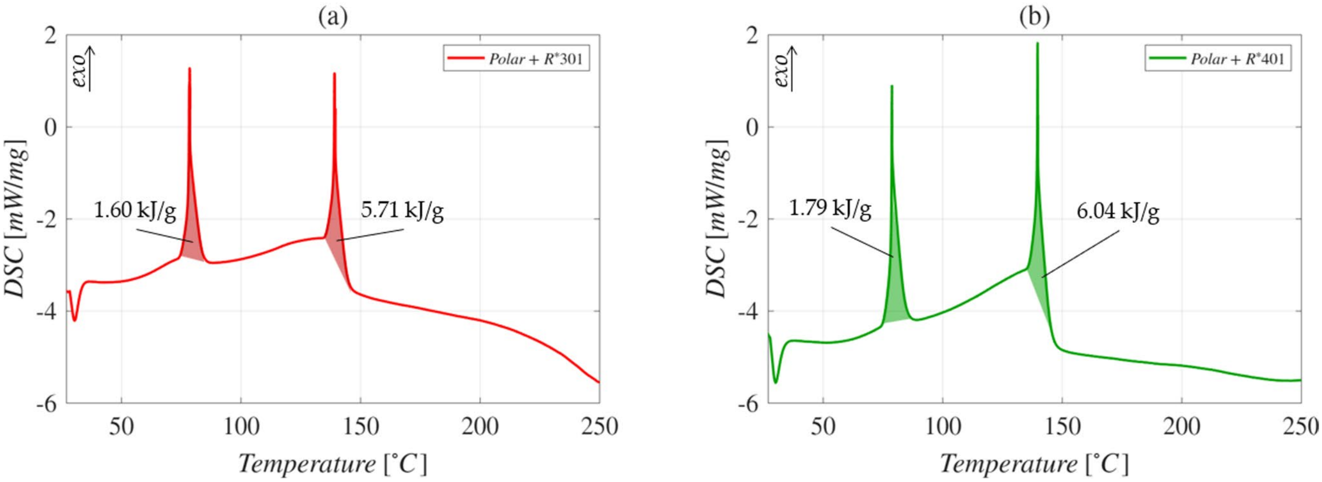

Fig. 7 DSC thermograms acquired for the two formulations PolarBear + R*301 (**a**) and PolarBear + R*401 (**b**) by simulating the *C2* curing cycle

premature vitrification; (ii) a post-cure at higher temperature (i.e., 120–180 °C) for completing the cross-linking, increases the T_g, and ensures optimal mechanical and thermal performance. Moreover, the presence of the two distinct exothermic events is consistent with the curing mechanism of epoxy–amine systems, where an initial chemically controlled reaction occurs at lower temperature by marking the beginning of cross-linking (likely involving one of the two $–NH_2$ groups), followed by a diffusion-controlled stage that requires higher thermal activation.

In the end, the curing efficiency of the two thermal cycles (*C1* and *C2*) was assessed by re-scanning the cured specimens. The acquired DSC thermograms are reported in Fig. 5b and c for *C1* and *C2*, respectively. When the curing cycle *C1* is implemented (see Fig. 5b), the exothermic peak was largely suppressed, although a small residual signal could still be observed, indicating that a fraction of reactive groups remained unreacted. Notably, formulation PolarBear + R*401 exhibited slightly higher residual heat than PolarBear + R*301, suggesting a marginally lower extent of cure under the same cycle. In contrast, after curing cycle *C2* (see Fig. 5c), both formulations showed no residual exothermic signal, confirming that a complete conversion was achieved. These observations demonstrate that while *C1* enables not fully complete curing, *C2* provides the necessary thermal input to fully cure both epoxy systems.

DMA Results

The results achieved for the T_g response using the DMA test for each investigated experimental scenario are reported in Table 5, whilst the tanδ versus temperature and storage modulus (*E'*) vs temperature curves are shown in Fig. 8.

The results obtained from the analysis of variance (ANOVA) conducted for the glass transition temperature (T_g) are shown in Table S2 of the supplementary materials. According to the obtained results, both the epoxy resin (*factor A*) and the curing cycle (*factor B*) are significantly influential on the T_g response, with p-values < 0.0001 for both. Additionally, the two factors are involved in a significant *interaction AB* (p-value < 0.0001). The results discussed until now are represented in the effects diagram shown in Fig. 9. The analysed model demonstrates good robustness in defining the variability of the observed response (T_g), as the R^2 value is 0.9982 (see Table S2 of the supplementary materials). Finally, the model adequacy check on the analysis residuals showed no anomalies.

Table 5 Glass transition temperature (T_g), storage modulus (*E'*) and cross-link densities (ν) values collected from DMA tests for the investigated epoxy latent resins

Sample	T_g [°C]	υ [mmol/cm^3]
P_R*301_C1	116.6 ± 0.3	0.74
P_R*301_C2	119.5 ± 0.1	1.56
P_R*401_C1	93.0 ± 0.8	0.73
P_R*401_C2	98.2 ± 0.2	0.81

According to the effects diagram shown in Fig. 9, it can be observed that the chosen curing cycle (*factor B*) has less influence on the PolarBear + R*301 formulation. In fact, moving from curing cycle *C1* to *C2* results in a T_g increase of 2.5%. Conversely, for the PolarBear + R*401 formulation, the *factor B* has a greater impact. Indeed, moving from the curing cycle *C1* to *C2* one results in an almost 5.6% increase in the T_g value. This result indicates that, by exploiting the curing cycle *C1*, some moieties have not yet reacted within the epoxy network and, therefore, to achieve an increase in the cross-linking density of the epoxy system, a more intense thermal curing (i.e., at 140°*C*) is necessary. Considering the data dispersion, it appears to be of comparable magnitude for each investigated scenario.

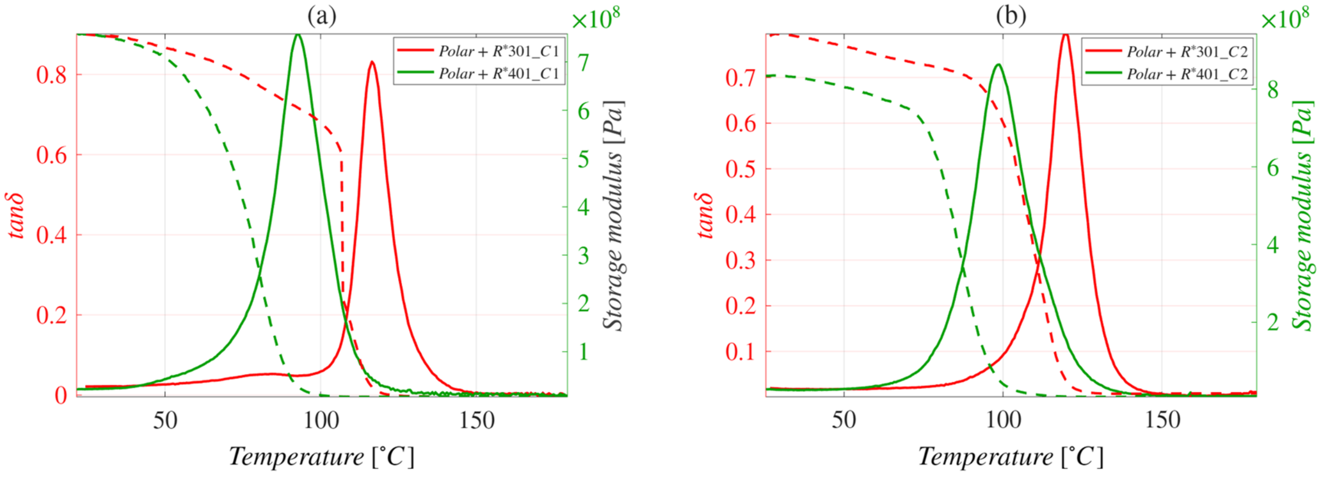

Fig. 8 Acquired tanδ versus temperature and E' vs temperature curves of the latent epoxy resins PolarBear + R*301 and PolarBear + R*401 cured via *C1* and *C2*

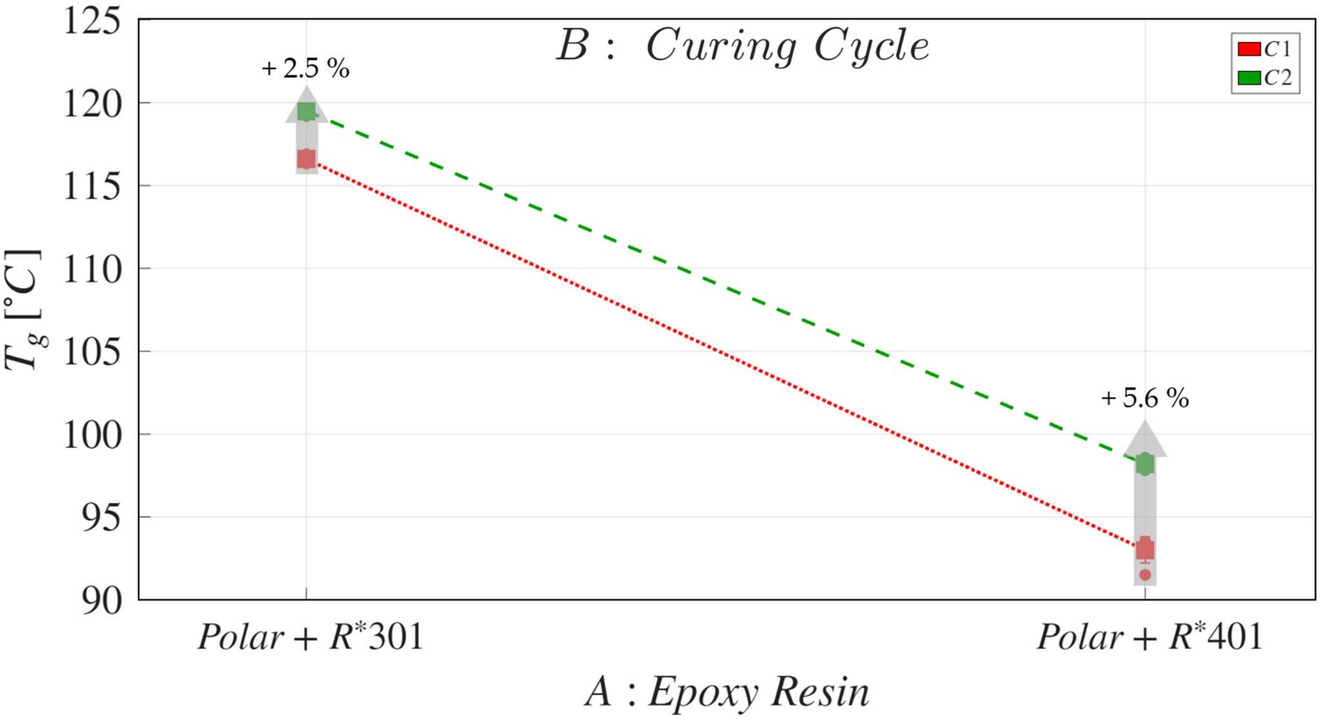

Fig. 9 Effects diagram for glass transition temperature (T_g)

Focusing on the storage modulus (E') determined via DMA tests, it ranged between 7.55E + 08 and 7.57E + 08 Pa when the epoxy resins are cured via *C1* curing cycle. While, the latter parameters ranged between 8.33E + 08 and 9.36E + 08 Pa when the epoxy resins are cured via *C2* curing cycle, thus confirming a higher cross-linking density (ν) achieved when the *C2* curing cycle is implemented. This result is consistent with the DSC analyses results already described in the Sect. "DSC results".

In conclusion, the latent-reactive epoxy system that provides the best T_g option is the system P_R*301_C2. When compared with previous results already reported in literature, the latter bio-based, fully-recyclable and latent epoxy system resulted to be placed in the mid-range among bio-based epoxy resins. While vanillin-based [79, 80] and eugenol-based [81] systems can achieve higher T_g values, i.e., up to 170–187 °C and over 200 °C, respectively, these systems are typically more brittle and require rigid aromatic structures, making them less flexible for tailored applications. Epoxidized soybean oil (ESO) [82] and epoxidized palm oil (EPO) [83] resins, derived from vegetable oils, generally achieve T_g values around 130–150 °C but suffer from plasticizing effects, which can reduce mechanical strength. Lignin-based systems, despite offering bio-contents up to 66%, often exhibit lower T_g values (about 79 °C) and variable processability due to lignin's structural complexity [84]. Thus, the pine oil-based resin's T_g of 120 °C, while not the highest, is sufficient for many industrial applications, especially where thermal cycling is limited. Furthermore, the 29% bio-content derive from pine oil together to its chemical recyclability reflect a strong foundation for sustainability, in contrast to vanillin, eugenol, and lignin-based epoxies which are irreversible thermosets, generally non-recyclable. Even ESO and EPO systems, despite some flexibility, do not yet offer reliable recycling under typical industrial conditions. Thus, the selected most performing epoxy system addresses a key limitation of conventional thermosets, regarding their end-of-life disposal, by offering a potential even for disassembly purposes. In addition to its recyclability, the proposed resin's latent curing mechanism represents a major processing advantage. The ability to delay crosslinking until activation via heat provides an extended working window, so allowing for precise material handling. This feature makes the system especially attractive for hybrid manufacturing approaches, where traditional composite lay-up techniques are merged with digital fabrication methods. In fact, during lay-up, the extended open time supports accurate positioning of fibers and metal inserts, essential for defect-free vacuum-assisted curing.

Flexural Test

The mechanical data collected from the flexural tests, i.e., the flexural strength, flexural modulus, and flexural strain at break for each investigated experimental scenario are reported in Table 6.

The results obtained from the ANOVA study conducted for the flexural strength are shown in Table S2 of the supplementary material. According to the obtained results, both the epoxy resin formulation (*factor A*) and the curing cycle (*factor B*) are significantly influential on the flexural strength (p-value = 0.0022 and p-value < 0.0001, respectively). The interaction effect (*AB*) between the two considered factors was found not to be significant (p-value = 0.0879 > 0.05). The analysed model demonstrates good robustness in defining the variability of the observed response, as R^2 = 0.9117 is high (see Table S3 of the supplementary material). Finally, the model adequacy check on the analysis residuals showed no anomalies.

Table 6 Results obtained from the flexural test (responses: flexural stress at break, flexural modulus and flexural strain at break)

Sample	Flexural Stress at Break [MPa]	Flexural Modulus [GPa]	Flexural Strain at Break [%]
P_R*301_C1	61.9 ± 4.3	2.8 ± 0.3	2.8 ± 0.3
P_R*301_C2	109.35 ± 4.5	2.5 ± 0.1	6.4 ± 0.4
P_R*401_C1	36.9 ± 2.1	2.6 ± 0.2	1.7 ± 0.1
P_R*401_C2	101.0 ± 6.4	3.2 ± 0.2	5.8 ± 0.1

Next, according to the effects diagram showed in Fig. 10, it can be observed that the curing cycle (*factor B*) has a decisive influence on the flexural response. In fact, moving from curing cycle *C1* to *C2* results in a flexural strength increase of about 76.6% for the PolarBear + R*301 epoxy formulation and up to 173.6% for the PolarBear + R*401 one. Conversely, the epoxy resin (*factor A*) has a smaller, though still significant, effect. Indeed, the PolarBear + R*301 formulation consistently exhibits higher strength compared to PolarBear + R*401 under identical curing conditions. These findings indicate that an adequate curing protocol is crucial to achieve a higher cross-linking density for the epoxy system, as also already confirmed by the results found from the DSC (see Sect. "DSC results") and DMA (see Sect. "DMA results") analyses. Considering the data dispersion, it appears to be of comparable magnitude for each investigated scenario.

Moving on, the results obtained from the analysis of variance (ANOVA) conducted for the flexural modulus are shown in Table S4 of the supplementary materials. According to the obtained results, the curing cycle (*factor B*) is significantly influential on the flexural modulus response (p-value = 0.0017 < 0.05). On the other hand, the epoxy resin (*factor A*) and the interaction effect (*AB*) were not found to be significant, with p-values of 0.8070 and 0.3911 (p-value > 0.05), respectively. The analysed model demonstrates fair good robustness in describing the variability of the observed response, as the R^2 value is 0.6990 (see Table S4 of the supplementary materials). Finally, the model adequacy check on the analysis residuals showed no anomalies.

According to the effects diagram shown in Fig. 11, the curing cycle (*factor B*) has a relevant impact on the flexural modulus. Moving from curing cycle *C1* to *C2* results in an increase of about 35.2% for the *PolarBear* + *R**301 formulation and about 21.8% for the *PolarBear* + *R**401 formulation. Conversely, the effect of the epoxy formulation (*factor A*) is negligible under identical curing conditions, which is consistent with the ANOVA results. These findings confirm that the flexural modulus is predominantly governed by the applied curing protocol, while the type of epoxy resin plays a secondary role. The dispersion of the experimental data appears to be of comparable magnitude across the different tested scenarios (see Fig. 12).

In the end, the results obtained from the ANOVA conducted for the flexural strain at break are shown in Table S5 of the supplementary material. According to the obtained results, both the epoxy resin (*factor A*) and the curing cycle (*factor B*) are significantly influential on the flexural strain,

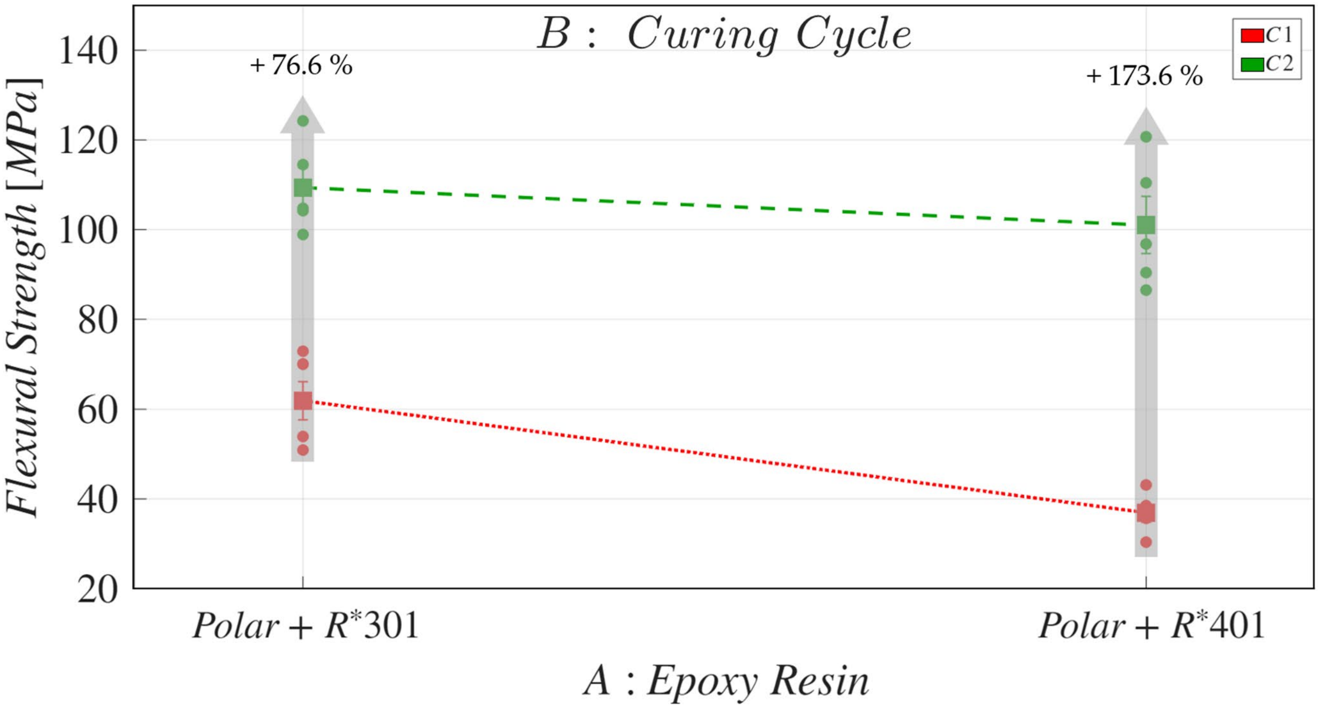

Fig. 10 Effects diagram for the flexural strength

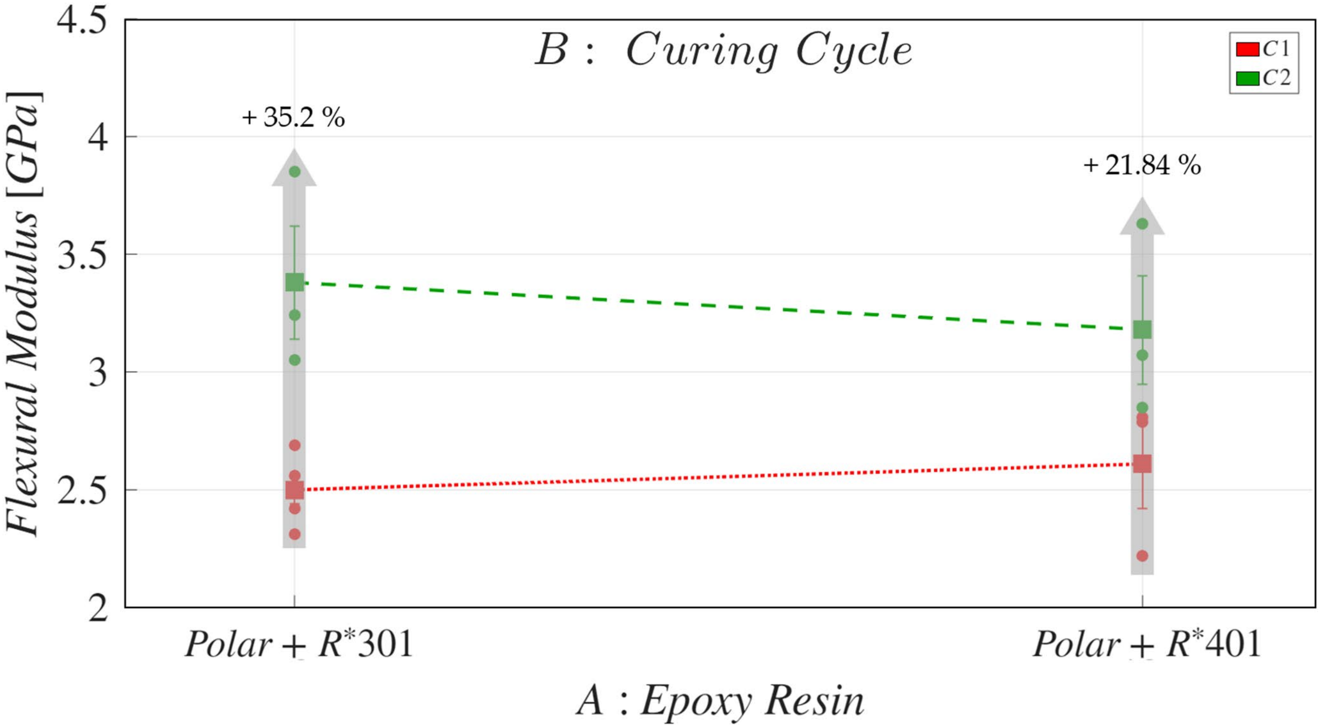

Fig. 11 Effects diagram for the flexural modulus

with p-values of 0.0002 and <0.0001, respectively. The interaction effect (AB) between the two investigated factors was not found to be significant (p-value$=0.5944>0.05$). The analysed model demonstrates excellent robustness in describing the variability of the observed response, as the $R^2 = 0.9650$ (see Table S5 of the supplementary material). Finally, once again the model adequacy check on the analysis residuals showed no anomalies.

Next, looking at the effects diagram shown in Fig. 12 , the curing cycle (*factor B*) has the most decisive influence on the flexural strain response. In fact, moving from curing cycle *C1* to *C2* results in an increase of about 124.7% for the PolarBear + R*301 formulation and up to 241.2% for the PolarBear + R*401 one. Conversely, the epoxy resin (*factor A*) also shows a statistically significant effect, although its impact is smaller compared to the curing protocol. These findings highlight the importance of curing conditions in enhancing ductility, with PolarBear + R*401 being particularly sensitive to the applied curing cycle. The dispersion of the experimental data appears to be of comparable magnitude across all tested conditions.

The results discussed until now were confirmed by the behavior of the acquired representative stress vs strain curves for the four investigated formulations (see Fig. 13).

According to Fig. 13 curves, it is worth nothing that the curing cycle exerts a dominant influence on both the flexural strength and strain responses. Samples cured under cycle *C1* (P_R301_C1 and P_R401_C1) exhibit lower flexural strength and limited strain at break, indicating premature failure and reduced ductility. In contrast, samples subjected to cycle C2 (P_R301_C2 and P_R401_C2) show significantly higher flexural strength values coupled with much greater strain at break, confirming the beneficial role of an intensified curing cycle.

Among the formulations, PolarBear + R*301 displays higher stiffness in the initial elastic region, whereas PolarBear + R*401 demonstrates slightly greater strain capacity under identical curing conditions. The combined analysis of these curves confirms that enhanced curing promotes a more efficient cross-linking within the epoxy matrix, leading to superior strength and ductility, in agreement with the ANOVA results discussed earlier.

Furthermore, the investigated latent epoxy resins demonstrate properties which are competitive with other commercial bio-based systems, as reported in Table 7, especially considering their recyclability and latent curing capabilities.

Thus, the investigated pine oil-based latent epoxy resins offer a balanced combination of mechanical performance, recyclability, and processing advantages, making it a promising candidate for sustainable hybrid metal/CFs composite joints applications.

Hybrid Joint Interfacial Properties

The results obtained from the SBS tests performed on the hybrid joints are summarized in Table 8, while a representative load vs displacement curve is shown in Fig. 14. The determined average ILSS was 11.9 ± 0.4 MPa, and the corresponding mean maximum load was 1429.2 ± 53.3 N. The representative curve (see Fig. 14) highlights a nearly linear elastic response up to the maximum load, followed by a sudden drop, indicating a brittle shear failure concentrated at the interface. When compared with benchmark values reported in the literature for hybrid joints and sandwich composites,

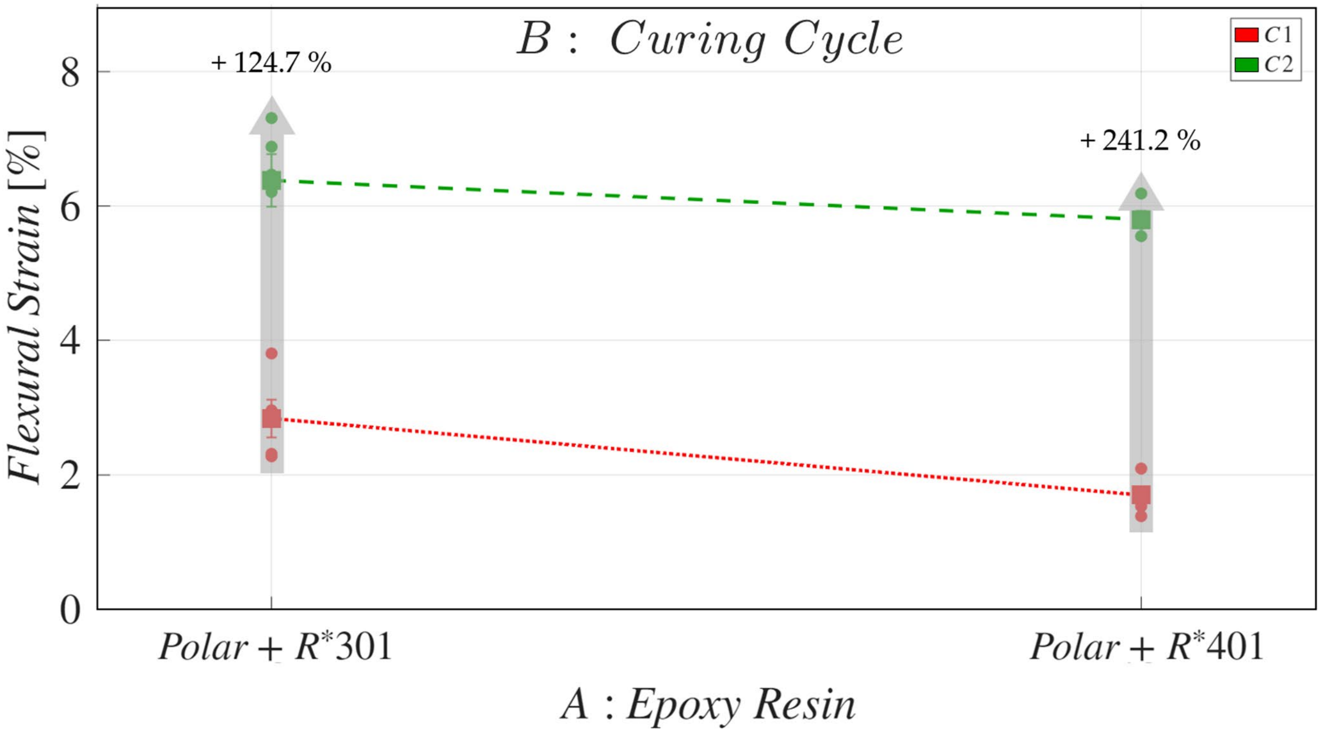

Fig. 12 Effects diagram for the flexural strain at break

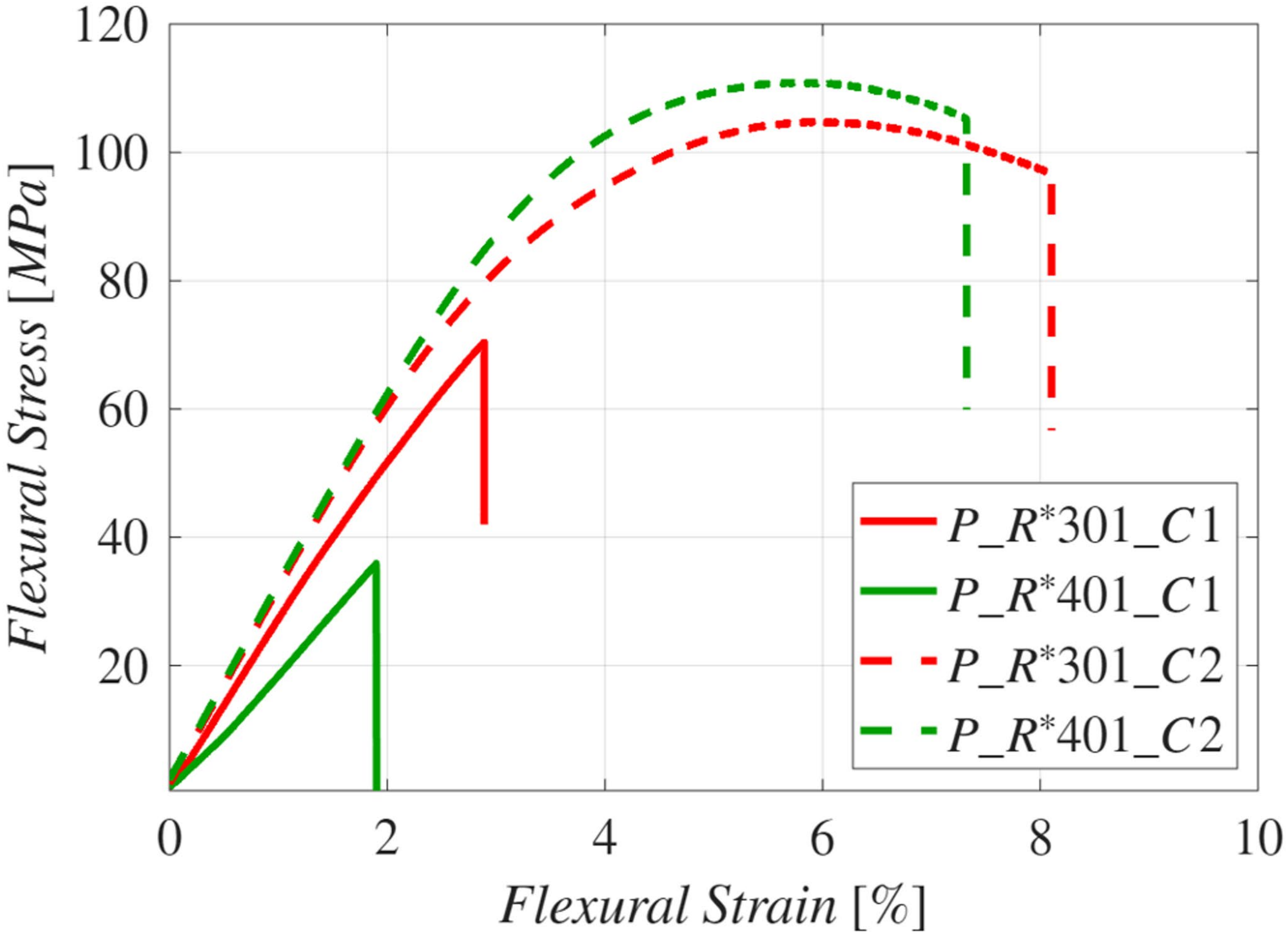

Fig. 13 Representative flexural stress vs flexural strain curves acquired for the four investigated epoxy formulations

which typically range between 5 and 30 MPa depending on constituent materials and interfacial treatments, the present system falls in the middle part of this spectrum. For instance, hybrid CFRP–metal joints have been shown to achieve ILSS values exceeding 20 MPa when advanced surface structuring or adhesion-promoting treatments are applied, whereas untreated or polymer–metal interfaces generally exhibit values close to or below 15 MPa [88].

Furthermore, representative micrographs of the hybrid joint are shown in Fig. 15, highlighting the morphology of the 316L insert/CFs composite and CFs composite/PVDF core interfaces. The cross-sectional overview in Fig. 15a shows the two distinct interfaces, with the metallic 316L insert/CFs composite interface (red dashed line) exhibiting a more irregular morphology compared to the smoother CFs composite/PVDF core interface (blue dashed line). At higher magnification (see Fig. 15b), the 316L insert/CFs composite region reveals evidence of mechanical interlocking, with epoxy resin penetrating into the surface asperities of the 3D printed steel plate. This feature contributes positively to load transfer, although local discontinuities and voids are visible along the interphase, which may act as crack initiators. In contrast, the CFs composite/PVDF core interface (see Fig. 15c) appears relatively smooth and continuous, but the presence of localized debonding sites and gaps indicates limited interfacial adhesion due to the lower chemical compatibility between PVDF core and epoxy resin. These observations are consistent with the SBS test results, which revealed a moderate interlaminar shear strength. The abrupt load drop seen in the representative load vs displacement curve (see Fig. 14) reflects brittle interfacial failure, in line with the discontinuities observed in both interfaces. In particular, the limited adhesion at the CFs composite/PVDF core boundary likely represents a weak link in the hybrid joint, while the partial mechanical interlocking at the 316L insert/CFs composite interface enhances strength but cannot fully compensate for interfacial defects. Together, the mechanical and microstructural results confirm that the interphase governs the failure mechanism of the system, suggesting that targeted surface modification strategies, such as plasma treatment of PVDF or tailored roughness of 316L insert, are required to improve shear performance and enhance overall

Table 7 Comparison of flexural mechanical properties of epoxy system P_R301_C2 with bio-based epoxy characterized in the state-of-the-art

Epoxy System	Flexural Strength [MPa]	Flexural Modulus [GPa]	T_g [°C]	Bio-based content [%]	Latency	Viscosity [mPa·s]	Ref.
FormuLITE 2 (Cardolite)	112.1	–	~ 80–120	~ 34–45	Latency not reported	Resin ~2200 (25 °C), hardener ~400 (25 °C)	[85]
FormuLITE 1 (Cardolite)	92.5	–	~ 80–120	~ 34–45	Latency not reported	Resin ~2200 (25 °C), hardener ~400 (25 °C)	[85]
FormuLITE 3 (Cardolite)	72.6	–	~ 80–120	~ 34–45	Latency not reported	Resin ~2200 (25 °C), hardener ~400 (25 °C)	[85]
Greenpoxy 56 (Sicomin) with SD 4772	72.0	3.5	~ 100	~ 45	Mix pot life ~60 min at 25 °C; cures 10 min at 100 °C	Resin ~1400 (20 °C)	[86]
Greenpoxy 56 (Sicomin) with SZ 8525	78.0	3.1	~ 100	~ 45	Pot life ~60 min; cures 10 min at 100 °C	Mixed system ~1160 (20 °C)	[86]
Greenpoxy 33 (Sicomin) with SZ 8525	80.0	3.0	~ 80–90	~ 30–35	Pot life ~60 min	~ 1100–1300 (25 °C)	[86]
ELO/TA (Epoxidized Linseed Oil/Tannic Acid)	72.0	3.0	~ 60–70	100	Latent at RT, thermally activated	~ 5000	[87]
Pine oil Recyclable Latent Epoxy	100–110	2.5–3.2	100–120	28	Latent curing	790–920 (25 °C)	This work

Table 8 Results obtained from the SBS test (responses: ILSS and maximum load)

Sample	ILSS [MPa]	Maximum Load [*N*]
I	11.9	1429.2
II	11.8	1410.8
III	11.5	1376.4
IV	13.5	1624.6
V	10.9	1304.8
Mean	11.9	1429.2
St. Err.	0.4	53.3

joint reliability. Alternatively, even exploiting metallic pins as part of the 3D printed metal component could act as interface with the composite by promoting enhanced interlocking [29, 30].

Recycled Products

Recycled Thermoplastics: Chemical, Thermal and Morphological Properties

Focusing on the chemical recycling of the epoxy resins, the recycling process yield resulted to be equal to almost 100% for the rTP301, as the entire epoxy matrix was recovered in the form of an oligomer. While, it was equal to 96% for the rTP401.

The acquired MALDI-TOF spectrum for the rTP301, reported in Fig. 16a, displays three predominant peaks that correspond to protonated oligomers with $n=2$, 3, and 4 repeating units (415 Da per unit). The first peak at m/z 831 is attributed to the proton adduct of the molecular structure reported in the inset of Fig. 16a. This assignment confirms the successful incorporation of cleavable epoxy fragments into oligomeric species of defined length.

While, the acquired MALDI-TOF spectrum for rTP401, illustrated in Fig. 16b, reveals a distinct series of peaks associated with oligomers containing 1 to 4 repeating units, each with a mass increment of 429 Da. The most intense signals correspond to oligomers with $n=2$–4 units. Similarly to R*301, the initial peak at m/z 519 is assigned to the proton adduct of the structure presented in the inset of Fig. 16b. These results demonstrate that the recycled material preserves well-defined oligomeric distributions, consistent with the expected fragmentation pathway of the cleavable epoxy precursors.

According to the GPC analysis results (see related chromatograms in Figure S1 of the supplementary materials), the determined molecular weight for the rTP301 and rTP401 is equal to 10200 and 12100 Da, respectively.

Next, the results collected for the T_g for the two recycled thermoplastics (rTP301 and rTP401) are reported in Table 9. Whilst, the acquired $tan\delta$ vs temperature curves are shown in Fig. 17.

The acquired TGA thermograms, reported in Figure S2 of the supplementary materials, are consistent with these results. In fact, the recycled thermoplastic rTP401 (green curve) begins its main mass loss slightly earlier (10–15 °C lower onset) and leaves a smaller char yield at 700 °C than rTP301 (red curve), while also showing a marginally larger low-temperature loss (<150 °C) attributable to adsorbed water/volatiles from its more polar end-groups.

The acquired ATR-FTIR spectra (see Figure S3 of the supplementary materials) confirmed that both recycled thermoplastics (rTP301 and rTP401) consist of hydroxyl- and amine-terminated BPA-ether oligomers, as shown by broad

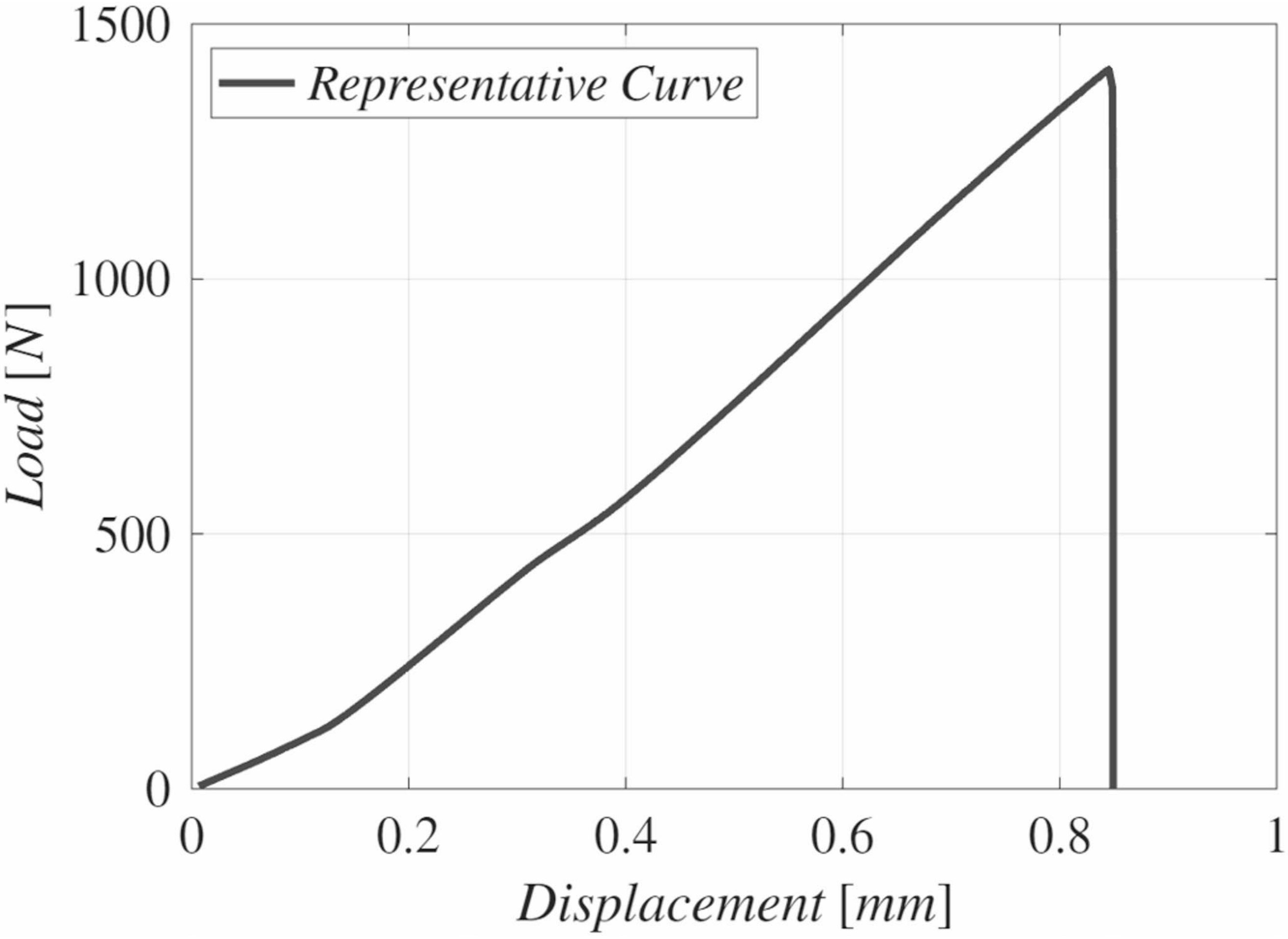

Fig. 14 Representative load vs. displacement curve acquired for the hybrid joint

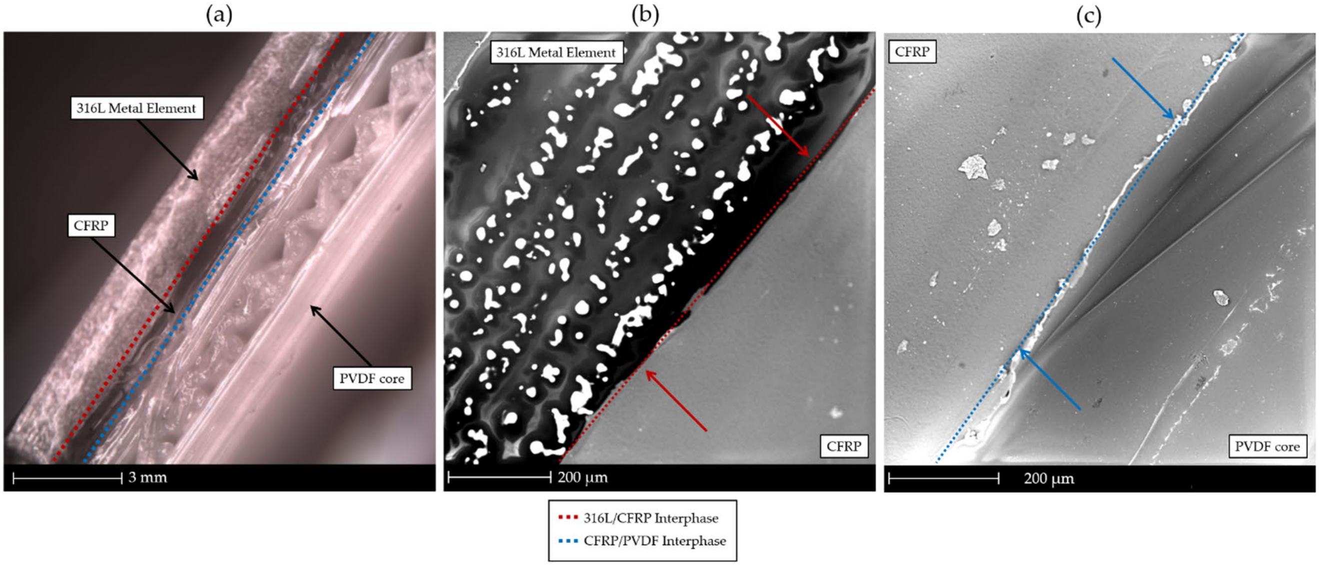

Fig. 15 Multiscale microstructural characterization of the hybrid 3D printed metal/CFRP/PVDF joint at 350× magnification. (**a**) Optical micrograph of the overall joint cross-section showing the 316L stainless steel insert, the carbon-fiber-reinforced polymer (CFRP) layer, and the PVDF core; the red and blue dashed lines indicate the 316 L/CFRP and CFRP/PVDF interphases, respectively. (**b**) Scanning electron micrograph of the 316 L/CFRP interphase highlighting the interfacial morphology and local material penetration (red arrows). (**c**) Scanning electron micrograph of the CFRP/PVDF interphase showing the continuity of the bonded interface and material interdiffusion (blue arrows)

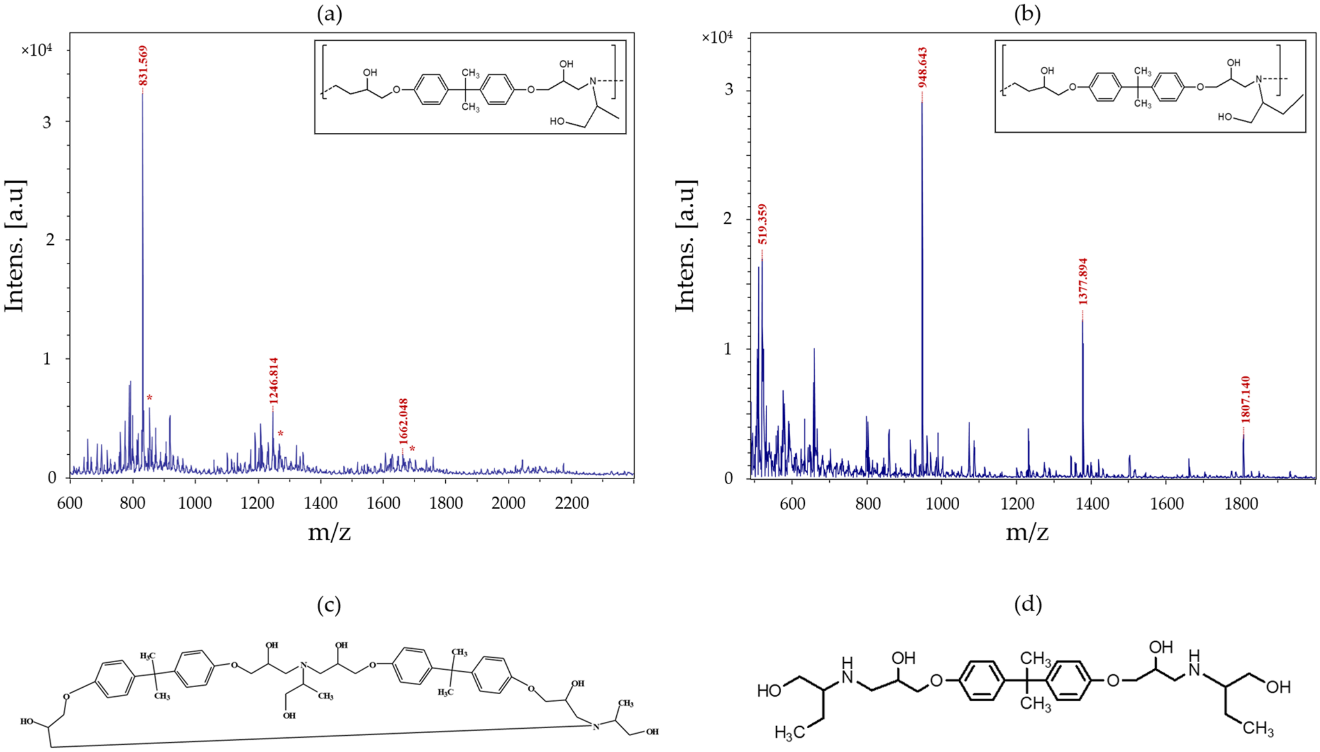

Fig. 16 MALDI-MS spectra of rTP301 (**a**) and rTP401 (**b**) recycled thermoplastics; within the insets are shown the corresponding repetitive unit's chemical structures. Dimeric structures with m/z 1662 and m/z 1038 hypothesized for rTP301 (**c**) and rTP401 (**d**), respectively

Table 9 T_g Values determined by DMA for the recycled thermoplastics rTP301 and rTP401

Sample	T_g[°C]
rTP301	51.3
rTP401	47.7

OH/NH bands (3600–3100 cm⁻¹), aromatic absorptions (~1600 and 1510 cm⁻¹), and strong ether signals (1180–1020 cm⁻¹), with no residual epoxy (910 cm⁻¹) or acetate/carboxylate features. rTP401 exhibited slightly stronger OH/NH and C–N/C–O bands, indicating a higher concentration of polar end-groups compared to rTP301. These chemical differences are consistent with its lower T_g (47 vs 51 °C) and broader tanδ peak (see Fig. 17), suggesting greater chain mobility and stronger hydrogen-bonding interactions, despite its slightly higher molecular weight from GPC.

SEM micrographs of the recycled thermoplastics are shown in Figure S4 of the supplementary materials. rTP301 appears as clean, angular particles with smooth fractured surfaces, reflecting efficient drying and the absence of agglomeration (see Figure S4a). In contrast, rTP401 shows compact agglomerates with visible impurities (see Figure S4b), which can be ascribed to its higher end-group density and polarity revealed by FTIR. These polar functionalities promote hydrogen bonding and retention of residual volatiles/impurities, in line with the broader tanδ peak and lower T_g observed by DMA, as well as the slightly earlier onset of thermal degradation in TGA.

Recycled CFs Characterization

The implemented disassembly procedure allowed to recover the used CFs with a recycling process yield equal to 100%. They were recovered as non-woven CFs, as shown in Fig. 2. The morphological analysis via SEM allowed to confirm that the implemented disassembly strategy did not negatively affect nor damage the surface of CFs, as highlighted from the acquired micrographs in Fig. 18a. Furthermore, it is worth of noting that the set parameters for the employed chemical recycling process allowed to almost fully dissolve the epoxy matrix, since the recycled CFs appeared quite clean. Similar outcomes were already found both for CFs and natural fibers in previous studies [39, 68]. This result was also confirmed by the performed thermogravimetric analysis. In fact, the TG thermogram reported in Fig. 18b confirms that the rCFs shows a total weight loss of about 8–9 wt% up to 600 °C, which can be attributed to residual organic species from the epoxy resin together with minor contributions from surface sizing and adsorbed moisture. This indicates that the recycling process efficiently removed more than 90 wt% of the matrix, leaving only a

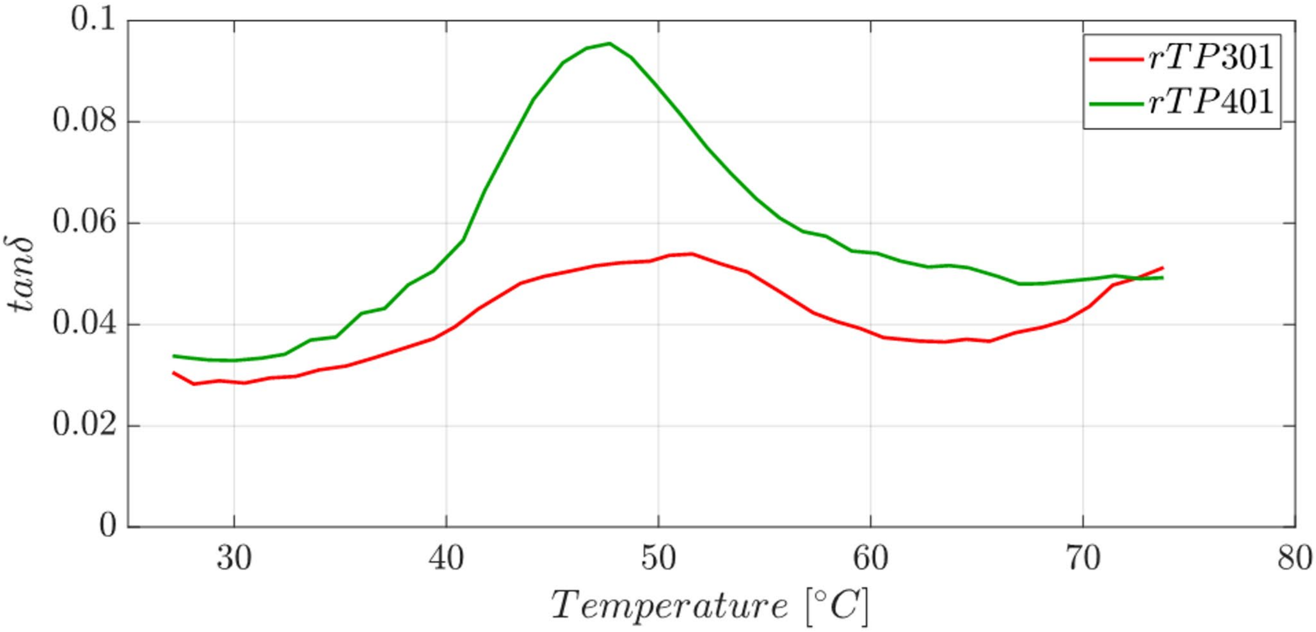

Fig. 17 Acquired tanδ versus temperature curves of the recycled thermoplastic rTP301 (red line) and rTP401 (green line)

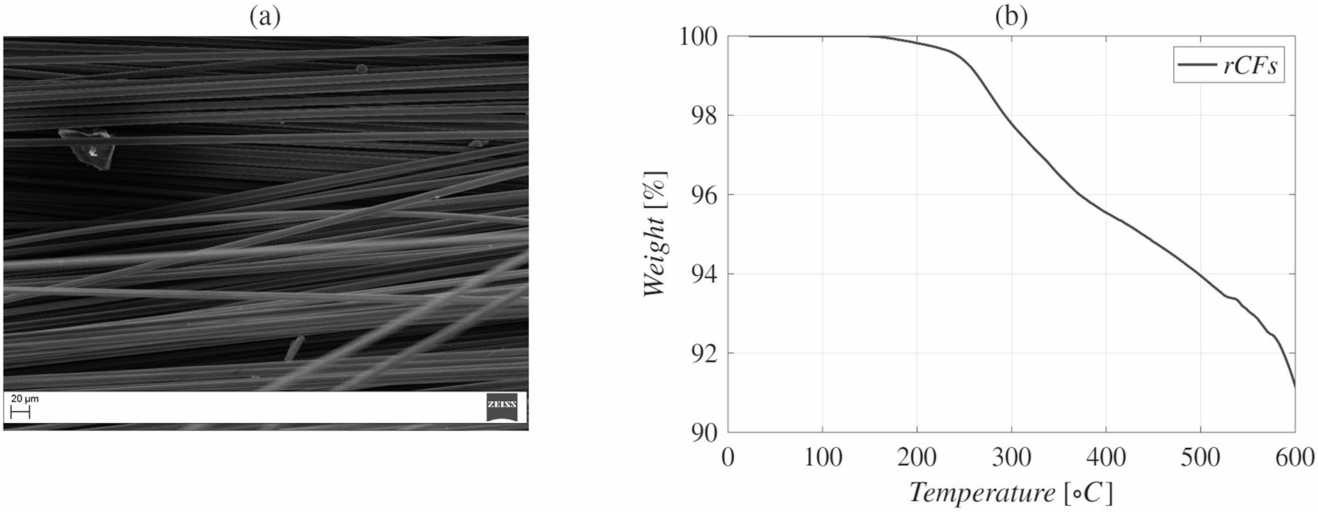

Fig. 18 (**a**) SEM micrographs (magnification of 500×) of the recycled CFs (**b**)

small fraction of epoxy-derived residues on the fiber surface. However, this issue can be overcame by making the dissolution process last slightly longer.

Recovered Metallic Components Characterization: FTIR-ATR

The FTIR-ATR acquired spectra for the virgin vs recovered 3D printed metallic components are reported in Fig. 15.

In accordance with the acquired spectra the 316L stainless steel FTIR spectrum is mostly flat with very low absorbance (see Fig. 19, red curve) as reported in the state-of-the-art [89]. While, the peaks found for the FTIR spectrum after recovering 316L from the epoxy-based composite using aqueous acetic acid are likely related to residual epoxy degradation products, adsorbed organics, or functional groups formed or retained during chemical recycling. In detail, the broad peak at 3410 cm^{-1} (area 1, see Fig. 19), which is related to stretching vibrations of molecular water and hydroxyl *O–H* groups [90], is due to adsorbed water from the recycling process; the peaks within the range 2950–2850 cm^{-1} (area 2, see Fig. 19), which are related to *C–H* stretching [91], indicates residual hydrocarbons, such as degraded epoxy fragments or leftover organic contaminants; the peaks within the range 1575–1375 cm^{-1} (area 3, see Fig. 19), which are related to aromatic $C = C$ and *C–H* bending, is characteristic of aromatic rings (from bisphenol

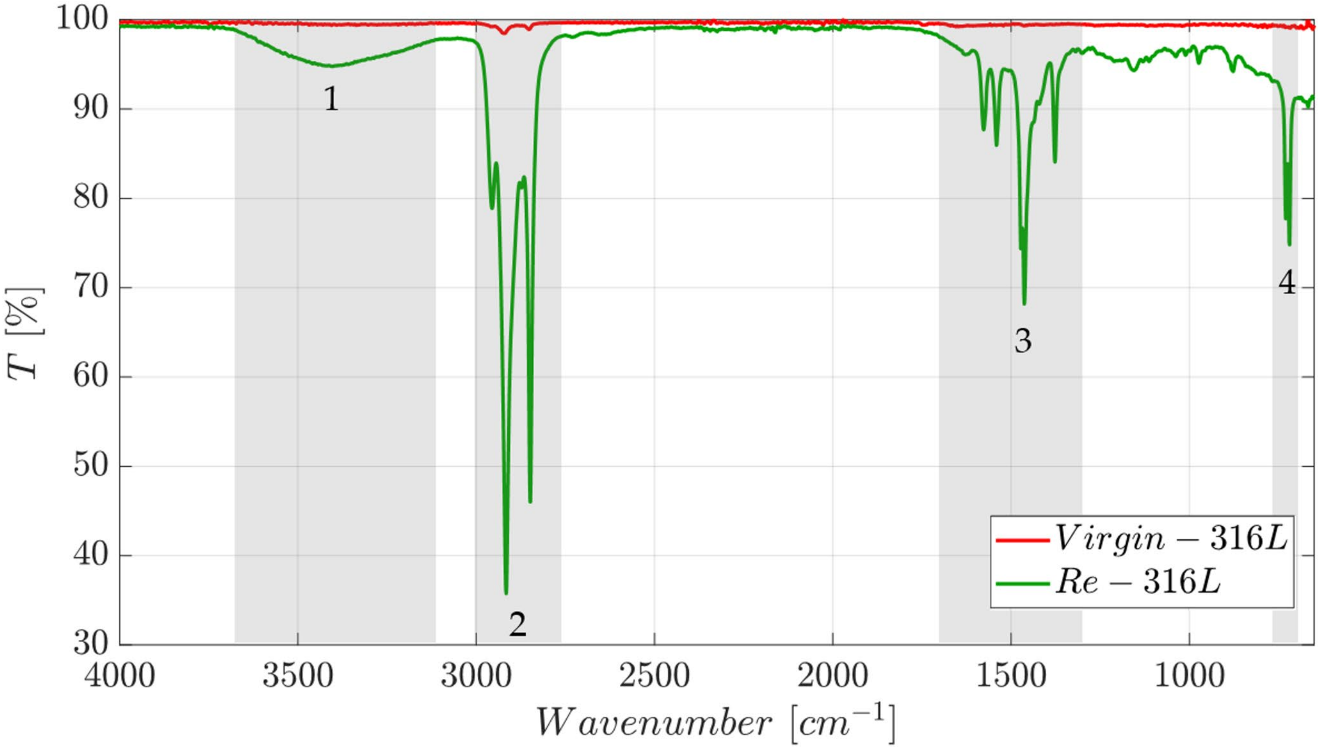

Fig. 19 FTIR-ATR spectra for the 316L components: virgin (red line) vs. recovered from the chemical recycling for disassembly (green line)

A in epoxy resin) and/or carboxylate groups (from partial oxidation or hydrolysis of epoxy or hardener residues) [92, 93]; the peaks at 720 cm^{-1} (area 4, see Fig. 19), which are related to CH_2 rocking (long-chain hydrocarbons), suggests presence of long aliphatic chains, i.e., potentially organic remnants from the epoxy matrix [93, 94]. Thus, to completely remove any contaminants and residual organics, further rinsing in solvents like ethanol/acetone [95, 96] or plasma cleaning approach [97] should be used as regenerative strategy for the recovered metal components.

Conclusions

This study focuses on the chemical, thermal and mechanical characterization of bio-based, recyclable and latent epoxy resins, engineered to meet high-performance mechanical and thermal specifications for advanced composite applications. The characterized latent epoxy resins exhibited glass transition temperature (T_g) values ranging between 90 and 120 °C, flexural strength and modulus values within the range of 35–110 MPa and 2.5–3.2 GPa, respectively, making them suitable for structural high-performance applications. Their recyclability was also assessed via chemical recycling, with a recycling process yield almost equal to 100% and recovering reusable recycled thermoplastics (rTP301 and rTP401) characterized by a T_g of about 50 °C.

One of the characterized latent epoxy resin, was employed in the fabrication of a hybrid joint comprising metal and CFs reinforced composites by combining AM and vacuum assisted hand lay-up fabrication techniques. Indeed, its latent behavior enabled the ability to delay cross-linking until activation via heat, so providing an extended working window and, in turn, allowing for precise material handling. This feature makes the system especially attractive for hybrid manufacturing approaches, where the extended open time supports accurate positioning of fibers and metal inserts. SBS tests on the hybrid joints yielded an average ILSS of about 11.9 MPa, hence placing the proposed design in a middle-spectrum comparable placement with literature benchmarks hybrid joints, justified by a good mechanical interlocking at the metal/CFs thermoset composite interface.

Furthermore, the implemented cleavable amine hardener (Recyclamine™ R*301) allowed to achieve the hybrid joints full recyclability, so enabling disassembly under controlled conditions, i.e., mild acid conditions. This property facilitated the full recovery of constituent raw materials (i.e., recycled polymer, recycled CFs, recovered metal inserts and 3D printed PVDF core), through a targeted chemical recycling process, achieving a recovery yield close to 100%. The proposed hybrid manufacturing strategy offers a sustainable alternative to conventional thermosets in composite manufacturing and end-of-life management.

Future work should explore the thermal and optical behavior of the developed hybrid, for example, to determine the CTE (Coefficient of Thermal Expansion) and RI (refractive index) values for the application of these structural components in electronics and advanced optical technologies. Next, the development of fully recyclable, bio-based epoxy/acrylate latent blends compatible with vat photopolymerization should be further explored to enable the fabrication of complex composite hybrid structures through digital and hybrid manufacturing approaches [73]. Recent studies have demonstrated the potential of such materials and techniques in the production of structural components for electric vehicle (EV) battery packs, where high precision, thermal stability, and design versatility are essential requirements [98]. Finally, it is recommended that future research efforts focus on scaling up production, assessing long-term durability, and exploring broader industrial applications, thereby bridging the gap between laboratory-scale developments and real-world sustainable composite manufacturing.

Supplementary Information The online version contains supplementary material available at https://doi.org/10.1007/s10924-026-03790-x.

Acknowledgements The research was partially funded by the MUR under the grant scheme PRIN with the project TARGET “addi-Tive mAnufactuRing for liGhtwEight joinTs” (grant number 2020E3XL47_003, CUP E63C20011220001), partially funded by the project “Sistemi innovativi di fabbricazione flessibile per materiali compositi ecocompatibili totalmente riciclabili” (RE-COMP) (Grant numbers CUP: B69J24001400005), and partially funded by the European Union (NextGeneration EU) and MUR-PNRR project Sicilian MicronanoTech Research And Innovation Center – SAMOTHRACE (CUP E63C22000900006), Spoke 1, WP 1.6.2.

Author Contributions L.S. wrote the main manuscript text, prepared the figures, formulated the epoxy resins, carried out the thermo-mechanical and morphological tests, the chemical recycling and analyzed the collected data via statistical analysis. S.D., V.G. and P.M.R. performed the chemical analysis. C.T. 3D printed the metal components. L.S. and C.T. fabricated and characterized the hybrid joint. G.C., I.B. and A.L. supervised the research activities, dealt with projects administration and funding acquisition. All the authors revised the manuscript.

Funding Open access funding provided by Università degli Studi di Catania within the CRUI-CARE Agreement

Data Availability Data will be made available on request.

Declarations

Conflict of interest The authors declare no conflict of interest.

References

1. Gohlke M, Schuldt T, Döringshoff K et al (2015) Adhesive bonding for optical metrology systems in space applications. J Phys Conf Ser 610:012039. https://doi.org/10.1088/1742-6596/610/1/012039
2. Khan MA, Aglietti GS, Crocombe AD et al (2018) Development of design allowables for the design of composite bonded double-lap joints in aerospace applications. Int J Adhes Adhes 82:221–232. https://doi.org/10.1016/J.IJADHADH.2018.01.011
3. Fiore V, Alagna F, Di Bella G, Valenza A (2013) On the mechanical behavior of BFRP to aluminum AA6086 mixed joints. Composites Part B: Engineering 48:79–87. https://doi.org/10.1016/J.COMPOSITESB.2012.12.009
4. Di Bella G, Borsellino C, Pollicino E, Ruisi VF (2010) Experimental and numerical study of composite T-joints for marine application. Int J Adhes Adhes 30:347–358. https://doi.org/10.1016/J.IJADHADH.2010.03.002
5. Osborne J (2013) Automotive composites – in touch with lighter and more flexible solutions. Met Finish 111:26–30. https://doi.org/10.1016/S0026-0576(13)70159-4
6. Czerwinski F (2021) Current trends in automotive lightweighting strategies and materials. Materials 14(21):6631. https://doi.org/10.3390/MA14216631
7. Taub AI, Luo AA (2015) Advanced lightweight materials and manufacturing processes for automotive applications. MRS Bull 40:1045–1053. https://doi.org/10.1557/MRS.2015.268/FIGURES/7
8. Wong WK, Lai CHN, Cheng WY et al (2022) Polymer–Metal composite healthcare materials: from nano to device scale. J Compos Sci 6(8):218. https://doi.org/10.3390/JCS6080218
9. Lambiase F, Scipioni SI, Lee CJ et al (2021) A state-of-the-art review on advanced joining processes for metal-composite and metal-polymer hybrid structures. Materials 14(8):1890. https://doi.org/10.3390/MA14081890
10. Zhao H, Zhang R, Bin Z (2018) A Review of Automotive Lightweight Technology. Advances in Engineering Research 59–62. https://doi.org/10.2991/MECAE-18.2018.10
11. Thoppul SD, Finegan J, Gibson RF (2009) Mechanics of mechanically fastened joints in polymer–matrix composite structures – a review. Compos Sci Technol 69:301–329. https://doi.org/10.1016/J.COMPSCITECH.2008.09.037
12. Yousefpour A, Hojjati M, Immarigeon JP (2004) Fusion bonding/welding of thermoplastic composites. J Thermoplast Compos Mater 17:303–341. https://doi.org/10.1177/0892705704045187
13. Stig F, Hallström S (2013) Influence of crimp on 3D-woven fibre reinforced composites. Compos Struct 95:114–122. https://doi.org/10.1016/J.COMPSTRUCT.2012.07.022
14. Umair M, Hamdani STA, Asghar MA et al (2018) Study of influence of interlocking patterns on the mechanical performance of 3D multilayer woven composites. J Reinf Plast Compos 37:429–440. https://doi.org/10.1177/0731684417751059
15. Adluru HK, Zhou E, Hoos KH et al (2023) Performance prediction of interlock woven composites by independent mesh method.

Compos Part A Appl Sci Manuf 165:107317. https://doi.org/10.1016/J.COMPOSITESA.2022.107317
16. Calabrese L, Cicala G, Di Bella G et al (2024) Optimisation of ultrasonic welding process of carbon/epoxy composites using Nylon-based or PES thermoplastic interlayers. Compos Part B Eng 275:111318. https://doi.org/10.1016/J.COMPOSITESB.2024.111318
17. Wei Y, Jin X, Luo Q et al (2024) Adhesively bonded joints – A review on design, manufacturing, experiments, modeling and challenges. Compos B Eng 276:111225. https://doi.org/10.1016/J.COMPOSITESB.2024.111225
18. Hu N, Shu L, Zheng X et al (2024) A review of modification methods, joints and self-healing methods of adhesive for aerospace. Sci Prog. https://doi.org/10.1177/00368504241242271
19. Arenas JM, Alía C, Blaya F, Sanz A (2012) Multi-criteria selection of structural adhesives to bond ABS parts obtained by rapid prototyping. Int J Adhes Adhes 33:67–74. https://doi.org/10.1016/J.IJADHADH.2011.11.005
20. White CC, Tan K, Wolf AT, Carbary LD (2010) Advances in structural silicone adhesives. Adv Struct Adhesive Bonding 66–95. https://doi.org/10.1533/9781845698058.1.66
21. Satyanarayana DVV, Eswara Prasad N (2017) Chap. 9 Nickel-Based superalloys D.V.V. Aerospace materials and material technologies 1. Aerosp Mater 1:199–228
22. Emin ÇETİN M (2022) Investigation of carbon nanotube reinforcement to polyurethane adhesive for improving impact performance of carbon fiber composite sandwich panels. Int J Adhes Adhes 112:103002. https://doi.org/10.1016/J.IJADHADH.2021.103002
23. Kim YJ, Choi SH, Lee SJ, Jang KS (2021) Latent curing, chemorheological, kinetic, and thermal behaviors of epoxy resin matrix for prepregs. Ind Eng Chem Res 60:6153–6161. https://doi.org/10.1021/ACS.IECR.1C00576
24. Maggiore S, Banea MD, Stagnaro P, Luciano G (2021) A review of structural adhesive joints in hybrid joining processes. Polymers 13:3961. https://doi.org/10.3390/POLYM13223961
25. Palmieri FL, Hudson TB, Smith AJ et al (2022) Latent cure epoxy resins for reliable joints in secondary-bonded composite structures. Compos Part B Eng 231:109603. https://doi.org/10.1016/J.COMPOSITESB.2021.109603
26. Naumann S, Buchmeiser MR (2014) Latent and delayed action polymerization systems. Macromol Rapid Commun 35:682–701. https://doi.org/10.1002/marc.201300898
27. Haneda T, Matsuno S, Yamamoto H et al (2021) Latency control of chemical reactions in polymerization of epoxy resins using a hydrogen bonding network. CrystEngComm 23:7717–7719. https://doi.org/10.1039/D1CE01163D
28. Reuther P, Dünnwald P, Tabatabai M et al (2022) Thermally controlled acceleration of epoxy resin curing through polymer-bound imidazole derivatives with high latency. ACS Appl Polym Mater 4:1150–1158. https://doi.org/10.1021/acsapm.1c01568
29. Raimondi L, Tomesani L, Zucchelli A (2024) Enhancing the robustness of hybrid metal-composite connections through 3D printed micro penetrative anchors. Appl Compos Mater 31:1275–1293. https://doi.org/10.1007/S10443-024-10224-1/FIGURES/10
30. Graziosi S, Cannazza F, Vedani M et al (2020) Design and testing of an innovative 3D-printed metal-composite junction. Additive Manuf 36:101311. https://doi.org/10.1016/J.ADDMA.2020.101311
31. Spaggiari A, Favali F (2022) Evaluation of polymeric 3D printed adhesively bonded joints: effect of joint morphology and mechanical interlocking. Rapid Prototyp J 28:1437–1451. https://doi.org/10.1108/RPJ-09-2021-0259/FULL/PDF
32. Belei C, Effertz PS, Meier B, Amancio-Filho ST (2023) Additive manufacturing of metal-polymer hybrid parts: the influence of as-printed LPBF surface roughness on the joint strength. Front Mater 10:1202281. https://doi.org/10.3389/FMATS.2023.1202281/BIBTEX
33. Abreu T, Leal RM, Leitão C, Galvão I (2024) Metal–polymer joining by additive manufacturing: effect of printing parameters and interlocking design. J Manuf Mater Process 8:228–228. https://doi.org/10.3390/JMMP8050228
34. Abdoli H, Diegel O, Bickerton S (2024) Surface topology modification using 3D printing techniques to enhance the interfacial bonding strength between polymer substrates and prepreg carbon fibre-reinforced polymers. Int J Adv Manuf Technol 131:1867–1878. https://doi.org/10.1007/S00170-024-13217-3/FIGURES/10
35. Zhou Z, Gao X, Zhang Y (2022) Research progress on characterization and regulation of forming quality in laser joining of metal and polymer, and development trends of lightweight automotive applications. Metals 12:1666. https://doi.org/10.3390/MET12101666
36. Saitta L, Dattilo S, Rizzo G et al (2025) Chemical recycling of bio-based epoxy matrices based on precursors derived from waste flour: recycled polymers characterization. Polymers 17:335. https://doi.org/10.3390/polym17030335
37. Dattilo S, Cicala G, Riccobene PM et al (2022) Full recycling and re-use of bio-based epoxy thermosets: chemical and thermomechanical characterization of the recycled matrices. Polymers 14:4828. https://doi.org/10.3390/polym14224828
38. Ferrari F, Esposito Corcione C, Striani R et al (2021) Fully recyclable bio-based epoxy formulations using epoxidized precursors from waste flour: thermal and mechanical characterization. Polymers (Basel) 13:2768. https://doi.org/10.3390/polym13162768
39. Tosto C, Saitta L, Barouni A et al (2024) Comparison of carbon-reinforced composites manufactured by vacuum assisted resin infusion with traditional and fully recyclable epoxy resins. Polym Compos 45:15649–15663. https://doi.org/10.1002/pc.28858
40. Saitta L, Rizzo G, Tosto C et al (2023) Chemical recycling of fully recyclable bio-epoxy matrices and reuse strategies: a cradle-to-cradle approach. Polymers 15:2809. https://doi.org/10.3390/polym15132809
41. Saitta L, Montalbano G, Corvaglia I et al (2023) Printability of a recycled thermoplastic obtained from a chemical recycling process of a fully-recyclable epoxy matrix: an upscaling re-use strategy. Macromol Symp. https://doi.org/10.1002/masy.202200188
42. Saitta L, Pergolizzi E, Tosto C et al (2022) Fully-Recyclable Epoxy Fibres Reinforced Composites (FRCs) for Maritime Field. Chemical Recycling and Re-Use Routes
43. Wang D, Sun H, Xu W et al (2025) Research progress on fiber reinforced Polymer/Metal hybrid structures for automotive applications. Polym Compos. https://doi.org/10.1002/PC.70706
44. Shen MY, Guo ZH, Feng WT (2023) A study on the characteristics and thermal properties of modified regenerated carbon fiber reinforced thermoplastic composite recycled from waste wind turbine blade spar. Compos Part B Eng 264:110878. https://doi.org/10.1016/J.COMPOSITESB.2023.110878
45. Dolganova I, Bach V, Rödl A et al (2022) Assessment of critical resource use in aircraft manufacturing. Circ Econ Sustain 2:1193–1212. https://doi.org/10.1007/s43615-022-00157-x
46. Hyvärinen M, Pylkkö M, Kärki T (2023) Closed-loop recycling and remanufacturing of polymeric aircraft parts. J Compos Sci 7:121. https://doi.org/10.3390/jcs7030121
47. Heibeck M, Rudolph M, Modler N et al (2021) Characterizing material liberation of multi-material lightweight structures from shredding experiments and finite element simulations. Miner Eng 172:107142. https://doi.org/10.1016/j.mineng.2021.107142
48. Meschut G, Janzen V, Olfermann T (2014) Innovative and highly productive joining technologies for multi-material lightweight

car body structures. J Mater Eng Perform 23:1515–1523. https://doi.org/10.1007/s11665-014-0962-3

49. Persad J, Rocke S (2022) Multi-material 3D printed electronic assemblies: a review. Results Eng 16:100730. https://doi.org/10.1016/j.rineng.2022.100730
50. Wang P, Li J, Yang J et al (2023) Enabling 3D multilayer electronics through the hybrid of vat photopolymerization and laser-activated selective metallization. Addit Manuf 74:103717. https://doi.org/10.1016/j.addma.2023.103717
51. Choi G-M, Jang K-S, Choi K-S et al (2021) Thermochemical mechanism of the epoxy-glutamic acid reaction with Sn-3.0 Ag-0.5 Cu solder powder for electrical joining. Polymers (Basel) 13:957. https://doi.org/10.3390/polym13060957
52. Kim WG, Chun H (2016) Cure properties of alkoxysilylated epoxy resin systems with hardeners for semiconductor packaging materials. Mol Cryst Liq Cryst 636:107–116. https://doi.org/10.1080/15421406.2016.1201388
53. An H, Liu Z, Tian Q et al (2019) Thermal behaviors of nanoparticle reinforced epoxy resins for microelectronics packaging. Microelectron Reliab 93:39–44. https://doi.org/10.1016/j.microrel.2019.01.002
54. Kim WG, Chun H (2013) Cure properties of naphthalene-based epoxy resin systems with hardeners and latent catalysts for semiconductor packaging materials. Mol Cryst Liq Cryst 579:39–49. https://doi.org/10.1080/15421406.2013.805071
55. Borthakur PP, Das A, Sahariah JJ et al (2025) Revolutionizing patient care: 3D printing for customized medical devices and therapeutics. Biomedical Mater Devices. https://doi.org/10.1007/s44174-025-00324-2
56. Mamo HB, Adamiak M, Kunwar A (2023) 3D printed biomedical devices and their applications: a review on state-of-the-art technologies, existing challenges, and future perspectives. J Mech Behav Biomed Mater 143:105930. https://doi.org/10.1016/j.jmbbm.2023.105930
57. Saniman MNF, Karumdin N, Jamaludin AS et al (2024) Optimizing 3D Printing Manufacturing Process for Sports Instrumentation Production. pp 417–429
58. Liou G-S, Lin P-H, Yen H-J et al (2010) Highly flexible and optical transparent 6F-PI/TiO2 optical hybrid films with tunable refractive index and excellent thermal stability. J Mater Chem 20:531–536. https://doi.org/10.1039/B916758G
59. Parola S, Julián-López B, Carlos LD, Sanchez C (2016) Optical properties of hybrid organic-inorganic materials and their applications. Adv Funct Mater 26:6506–6544. https://doi.org/10.1002/adfm.201602730
60. Saitta L, Cutuli E, Celano G et al (2023) A regression approach to model refractive index measurements of novel 3D printable photocurable resins for micro-optofluidic applications. Polymers 15:2690. https://doi.org/10.3390/POLYM15122690
61. Lebeau B, Innocenzi P (2011) Hybrid materials for optics and photonics. Chem Soc Rev 40:886. https://doi.org/10.1039/c0cs00106f
62. Cutuli, Emanuela, et al. "Effect of Build Orientation on Surface Finish and Hydrodynamic Stability of Inkjet 3D-Printed Microfluidic Channels." Polymers 17.13 (2025): 1864.
63. Cutuli E, Sanalitro D, Stella G et al (2023) A 3D-printed micro-optofluidic chamber for fluid characterization and microparticle velocity detection. Micromachines 14:2115. https://doi.org/10.3390/mi14112115
64. Saitta L, Cutuli E, Celano G et al (2024) Monolithic 3D Printed Micro-Optofluidic Device for Two-phase Flow Monitoring and Bioapplications. In: 2024 IEEE International Conference And Exposition On Electric And Power Engineering (EPEi). IEEE, pp 642–647
65. Saitta L, Cutuli E, Celano G et al (2023) Projection micro-stereolithography to manufacture a biocompatible micro-optofluidic device for cell concentration monitoring. Polymers. https://doi.org/10.3390/polym15224461
66. Cutuli E, Stella G, Guarino F, Bucolo M (2025) Automatic label-free image-based system for cell viability monitoring on-a-chip. Biomed Signal Process Control 106:107768. https://doi.org/10.1016/j.bspc.2025.107768
67. Forward AM, Ultrafuse 316L 3D Printer Metal Filament. https://forward-am.com/material-portfolio/ultrafuse-filaments-for-fused-filaments-fabrication-fff/metal-filaments/ultrafuse-316l/. Accessed 25 Apr 2025
68. Saitta L, Prasad V, Tosto C et al (2022) Characterization of bio-based epoxy resins to manufacture eco-composites showing recycling properties. Polym Compos. https://doi.org/10.1002/pc.27095
69. Gabbott P (2008) Principles and Applications of Thermal Analysis. Blackwell Publishing Ltd
70. Flory PJ (1944) Thermodynamics of heterogeneous polymers and their solutions. J Chem Phys 12:425–438. https://doi.org/10.1063/1.1723887
71. Flory PJ (1942) Thermodynamics of high polymer solutions. J Chem Phys 10:51–61. https://doi.org/10.1063/1.1723621
72. Saitta L, Rizzo G, Tosto C et al (2025) Development and thermo-mechanical analysis of bio-based epoxy resin/cardanol blends as matrices for green composites manufacturing. J Polym Environ 33:1561–1584. https://doi.org/10.1007/s10924-024-03486-0
73. Tosto C, Saitta L, Latteri A, Blanco I (2024) Development of recyclable bio-based epoxy/acrylate blends for liquid crystal display 3D printing. J Therm Anal Calorim. https://doi.org/10.1007/s10973-024-13094-8
74. Mahlin D, Wood J, Hawkins N et al (2009) A novel powder sample holder for the determination of glass transition temperatures by DMA. Int J Pharm 371:120–125. https://doi.org/10.1016/j.ijpharm.2008.12.039
75. Carlier V, Sclavons M, Legras R (2001) Supported dynamic mechanical thermal analysis: an easy, powerful and very sensitive technique to assess thermal properties of polymer, coating and even nanocoating. Polym (Guildf) 42:5327–5335. https://doi.org/10.1016/S0032-3861(00)00915-0
76. Tosto C, Tirillò J, Sarasini F et al (2022) Fused deposition modeling parameter optimization for cost-effective metal part printing. Polymers 14:3264. https://doi.org/10.3390/polym14163264
77. Tosto C, Saitta L, Barbagallo R et al (2024) Optimizing Dimensional Accuracy in Metal Fused Filament Fabrication: A Study on Shrinkage Prediction for 316L Parts. In: 2024 IEEE International Conference And Exposition On Electric And Power Engineering (EPEi). IEEE, pp 648–651
78. Dubey PK, Mahanth SKRECYCLAMINE, $^{®}$-NOVEL AMINE BUILDING BLOCKS FOR A SUSTAINABLE WORLD
79. Yu Q, Peng X, Wang Y et al (2019) Vanillin-based degradable epoxy vitrimers: reprocessability and mechanical properties study. Eur Polym J 117:55–63. https://doi.org/10.1016/j.eurpolymj.2019.04.053
80. Nabipour H, Niu H, Wang X et al (2021) Fully bio-based epoxy resin derived from vanillin with flame retardancy and degradability. React Funct Polym 168:105034. https://doi.org/10.1016/j.reactfunctpolym.2021.105034
81. Wan J, Zhao J, Gan B et al (2016) Ultrastiff biobased epoxy resin with high Tg and low permittivity: from synthesis to properties. ACS Sustain Chem Eng 4:2869–2880. https://doi.org/10.1021/acssuschemeng.6b00479
82. Chen Y, Yang L, Wu J et al (2013) Thermal and mechanical properties of epoxy resin toughened with epoxidized soybean oil. J Therm Anal Calorim 113:939–945. https://doi.org/10.1007/s10973-012-2859-4

83. Tan SG, Chow WS (2010) Thermal properties of anhydride-cured bio-based epoxy blends. J Therm Anal Calorim 101:1051–1058. https://doi.org/10.1007/s10973-010-0751-7
84. Gioia C, Colonna M, Tagami A et al (2020) Lignin-based epoxy resins: unravelling the relationship between structure and material properties. Biomacromolecules 21:1920–1928. https://doi.org/10.1021/acs.biomac.0c00057
85. Naik N, Shivamurthy B, Thimmappa BHS et al (2022) Bio-based epoxies: mechanical characterization and their applicability in the development of eco-friendly composites. J Compos Sci 6:294. https://doi.org/10.3390/jcs6100294
86. Iadarola A, Di Matteo P, Ciardiello R et al (2025) Mechanical characterization of cardanol Bio-Based epoxy resin blends: effect of different Bio-Contents. Polym (Basel) 17:296. https://doi.org/10.3390/polym17030296
87. Reinhardt N, Breitsameter JM, Drechsler K, Rieger B (2022) Fully bio-based epoxy thermoset based on epoxidized linseed oil and tannic acid. Macromol Mater Eng. https://doi.org/10.1002/mame.202200455
88. Abdoli H, Chan YL, Diegel O et al (2023) Enhancing the interfacial bonding strength between 3D-printed aluminium substrates and carbon fibre-reinforced polymers. Int J Adv Manuf Technol. https://doi.org/10.1007/s00170-023-11200-y
89. Vasconcelos DCL, Costa VC, Nunes EHM et al (2011) Infrared spectroscopy of Titania sol-gel coatings on 316L stainless steel. Materials Sciences and Applications 02:1375–1382. https://doi.org/10.4236/msa.2011.210186
90. Wood DL, Rabinovich EM, Johnson DW et al (1983) Preparation of high-silica glasses from colloidal gels: III, infrared spectrophotometric studies. J Am Ceram Soc 66:693–699. https://doi.org/10.1111/j.1151-2916.1983.tb10531.x
91. Pannico M, Mensitieri G, Musto P (2024) In-situ FTIR spectroscopy of epoxy resin degradation: kinetics and mechanisms. Front Chem. https://doi.org/10.3389/fchem.2024.1476965
92. Lin SC, Bulkin BJ, Pearce EM (1979) Epoxy resins. III. Application of fourier transform IR to degradation studies of epoxy systems. J Polym Science: Polym Chem Ed 17:3121–3148. https://doi.org/10.1002/pol.1979.170171006
93. González MG, Cabanelas JC, Baselga J (2012) Applications of FTIR on epoxy Resins - Identification, monitoring the curing Process, phase separation and water uptake. In: Infrared Spectroscopy - Materials Science, Engineering and Technology. InTech
94. Salasinska K, Barczewski M, Aniśko J et al (2021) Comparative study of the reinforcement type effect on the thermomechanical properties and burning of epoxy-based composites. J Compos Sci 5:89. https://doi.org/10.3390/jcs5030089
95. Brachmann E, Seifert M, Oswald S et al (2017) Evaluation of surface cleaning procedures for CTGS substrates for SAW technology with XPS. Materials 10:1373. https://doi.org/10.3390/ma10121373
96. Zaniboni JF, de Souza V, Escalante-Otárola WG et al (2022) Cleaning and microstructural effects of amyl acetate on pulp chamber dentin impregnated with epoxy resin-based endodontic sealer. J Esthet Restor Dent 34:1282–1289. https://doi.org/10.1111/jerd.12966
97. Lin A-D, Kung C-L, Hsieh W-C et al (2018) Study on cleaning the surface of stainless steel 316 using plasma electrolysis technology. Appl Sci 8:1060. https://doi.org/10.3390/app8071060
98. Photocentric 3D Printing Batteries https://photocentricgroup.com/3d-batteries/. Accessed 25 Apr 2025